

THESIS FOR THE DEGREE OF DOCTOR OF PHILOSOPHY

# Exciting Neutron-rich Nuclei

Radioactive beam experiments in complete kinematics

SIMON LINDBERG



Department of Physics  
CHALMERS UNIVERSITY OF TECHNOLOGY  
Göteborg, Sweden 2018

Exciting Neutron-rich Nuclei  
Radioactive beam experiments in complete kinematics  
SIMON LINDBERG  
ISBN 978-91-7597-764-5

©SIMON LINDBERG, 2018

Doktorsavhandlingar vid Chalmers tekniska högskola  
Ny serie nr 4445  
ISSN 0346-718X

Department of Physics  
Chalmers University of Technology  
SE-412 96 Göteborg  
Sweden  
Telephone +46 (0)31-772 10 00

Cover:

Identification plot of outgoing fragments in the SAMURAI setup, with the condition that the incoming ion is identified as  $^{30}\text{Ne}$ . This was used to identify possible events where unbound  $^{29}\text{Ne}$  nuclei had been produced and the original figure, including axis and labels, is found as Fig. 4.1 in this thesis.

Chalmers Reproservice  
Göteborg, Sweden 2018

Exciting Neutron-rich Nuclei  
Radioactive beam experiments in complete kinematics  
SIMON LINDBERG  
Department of Physics  
Chalmers University of Technology

## Abstract

Atoms are the building blocks which make up our world. Their stability depends on the atomic nucleus, consisting of protons and neutrons. Nuclei are complex many-body quantum mechanical systems governed by the nucleon-nucleon interaction. The complexity and the intricate nature of the nucleon-nucleon interaction so far prevented the description of all existing nuclei by a single model. Furthermore, nuclei and nuclear reactions in stars and stellar explosions play a key role in astrophysics. This motivates experiments to improve our understanding of nuclei and their role in the cosmos.

In this thesis I present results from experiments in complete kinematics performed at the radioactive beam facilities RIKEN and GSI/FAIR. The focus is on the first measurement of unbound states in  $^{29}\text{Ne}$ , that were studied using neutron knockout reactions from  $^{30}\text{Ne}$ . The invariant-mass spectrum shows two peaks, one at around 0.5 MeV and another one at 1.3 MeV. Moreover, results from an overview experiment, investigating light neutron-rich nuclei, between  $3 < Z < 10$ , are also presented. The results cover proton-removal cross sections in boron and carbon, important for designing future experiments, and unbound states in  $^{26}\text{F}$  where the first unbound states are observed at the relative energy 323 keV. Furthermore, the structure of the unbound nucleus  $^{13}\text{Be}$ , which is important for its bridging role between the bound  $^{12}\text{Be}$  and the Borromean halo nucleus  $^{14}\text{Be}$ , is studied. Also measurements on Coulomb dissociation of  $^{20,21}\text{N}$  and  $^{18}\text{C}$  are presented which allow to improve our understanding of r-process nucleosynthesis.

**Keywords:** Unbound States, Radioactive Beams, RIKEN, R<sup>3</sup>B, GSI, FAIR



---

## Acknowledgements

There are many people who have helped and supported me during the years, without whom I could not have produced this work.

I especially want to thank my supervisor, Andreas Heinz. Your support and passion to explain and discuss all possible problems and questions during the years have been invaluable.

I also want to thank Håkan Johansson for technical support and fruitful discussions. Thomas Nilsson for support and input in the analysis work. Of course, I also want to thank the rest of the people in the subatomic physics group creating a good working environment.

The experiments could not have been performed alone, hence I want to thank everybody who made the experiments I have taken part in possible. This includes the people at RIKEN, GSI/FAIR and ISOLDE. I especially want to thank Takashi Nakamura for inviting me to stay at the Tokyo Institute of Technology during a month, this was very helpful in the analysis work. Yosuke Kondo have been very helpful in answering questions concerning my analysis of  $^{29}\text{Ne}$ . Also Julian Kahlbow, Masahiro Yasuda and Aldric Revel have contributed with useful input to my work.

I also want to thank all my friends and family. Even though I not always have been able to explain in an understandable way what I am doing, you have always supported me. Finally I wish to thank Ronja, for believing in me and making my life much more joyful.



# List of Publications

This thesis is based on the following appended papers:

- I. R. Thies, A. Heinz, T. Adachi, Y. Aksyutina, J. Alcantara-Núñez, S. Altstadt, H. Alvarez-Pol, N. Ashwood, T. Aumann, V. Avdeichikov, M. Barr, S. Beceiro-Novo, D. Bemmerer, J. Benlliure, C. A. Bertulani, K. Boretzky, M. J. G. Borge, G. Burgunder, M. Camacho, C. Caesar, E. Casarejos, W. Catford, J. Cederkäll, S. Chakraborty, M. Chartier, L. V. Chulkov, D. Cortina-Gil, R. Crespo, U. Datta, P. Díaz Fernández, I. Dillmann, Z. Elekes, J. Enders, O. Ershova, A. Estradé, F. Farinon, L. M. Fraile, M. Freer, M. Freudenberger, H. O. U. Fynbo, D. Galaviz, H. Geissel, R. Gernhäuser, K. Göbel, P. Golubev, D. Gonzalez Diaz, J. Hagdahl, T. Heftrich, M. Heil, M. Heine, A. Henriques, M. Holl, G. Ickert, A. Ignatov, B. Jakobsson, H. T. Johansson, B. Jonson, N. Kalantar-Nayestanaki, R. Kanungo, R. Knöbel, T. Kröll, R. Krücken, J. Kurcewicz, N. Kurz, M. Labiche, C. Langer, T. Le Bleis, R. Lemmon, O. Lepyoshkina, **S. Lindberg**, J. Machado, J. Marganec, V. Maroussov, M. Mostazo, A. Movsesyan, A. Najafi, T. Nilsson, C. Nociforo, V. Panin, S. Paschalis, A. Perea, M. Petri, S. Pietri, R. Plag, A. Prochazka, A. Rahaman, G. Rastrepina, R. Reifarth, G. Ribeiro, M. V. Ricciardi, C. Rigollet, K. Riisager, M. Röder, D. Rossi, J. Sanchez del Rio, D. Savran, H. Scheit, H. Simon, O. Sorlin, V. Stoica, B. Streicher, J. T. Taylor, O. Tengblad, S. Terashima, Y. Togano, E. Uberseder, J. Van de Walle, P. Velho, V. Volkov, A. Wagner, F. Wamers, H. Weick, M. Weigand, C. Wheldon, G. Wilson, C. Wimmer, J. S. Winfield, P. Woods, D. Yakorev, M. V. Zhukov, A. Zilges, and K. Zuber, “Systematic investigation of projectile fragmentation using beams of unstable B and C isotopes,” *Phys. Rev. C*, vol. 93, p. 054601, May 2016.
- II. G. Ribeiro, E. Nácher, O. Tengblad, P. D. Fernández, Y. Aksyutina, H. Alvarez-Pol, L. Atar, T. Aumann, V. Avdeichikov, S. Beceiro-Novo, D. Bemmerer, J. Benlliure, C. A. Bertulani, J. M. Boillos, K. Boretzky, M. Borge, M. Caamano, C. Caesar, E. Casarejos, W. Cat-

---

ford, J. Cederkäll, M. Chartier, L. Chulkov, D. Cortina-Gil, E. Cravo, R. Crespo, U. D. Pramanik, I. Dillmann, Z. Elekes, J. Enders, O. Ershova, A. Estrade, F. Farinon, L. M. Fraile, M. Freer, H. Fynbo, D. Galaviz, H. Geissel, R. Gernhäuser, P. Golubev, K. Göbel, J. Hagdahl, T. Heftrich, M. Heil, M. Heine, A. Heinz, A. Henriques, M. Holl, A. Hufnagel, A. Ignatov, H. Johansson, B. Jonson, N. Kalantar-Nayestanaki, R. Kanungo, A. Kelic-Heil, N. Kurz, T. Kröll, M. Labiche, C. Langer, T. L. Bleis, R. Lemmon, **S. Lindberg**, J. Machado, J. Marganiec, A. Movsesyan, T. Nilsson, C. Nociforo, V. Panin, S. Paschalis, A. Perea, M. Petri, S. Pietri, R. Plag, R. Reifarth, C. Rigollet, K. Rissager, D. Rossi, M. Röder, D. Savran, H. Scheit, H. Simon, O. Sorlin, I. Syndikus, J. Taylor, R. Thies, P. Velho, A. Wagner, F. Wamers, M. Vandebrout, H. Weick, C. Wheldon, G. Wilson, C. Wimmer, J. Winfield, P. Woods, M. Zhukov, A. Zilges, and K. Zuber, “Structure of  $^{13}\text{Be}$  studied in proton knockout from  $^{14}\text{B}$ ,” in manuscript, submitted.

- III.** M. Vandebrout, A. Lepailleur, O. Sorlin, T. Aumann, C. Caesar, M. Holl, V. Panin, F. Wamers, S. R. Stroberg, J. D. Holt, F. de Oliveira Santos, H. Alvarez-Pol, L. Atar, V. Avdeichikov, S. Beceiro-Novo, D. Bemmerer, J. Benlliure, C. A. Bertulani, S. K. Bogner, J. M. Boillos, K. Boretzky, M. J. G. Borge, M. Caamaño, E. Casarejos, W. Catford, J. Cederkäll, M. Chartier, L. Chulkov, D. Cortina-Gil, E. Cravo, R. Crespo, U. Datta Pramanik, P. Díaz Fernández, I. Dillmann, Z. Elekes, J. Enders, O. Ershova, A. Estradé, F. Farinon, L. M. Fraile, M. Freer, D. Galaviz, H. Geissel, R. Gernhäuser, J. Gibelin, P. Golubev, K. Göbel, J. Hagdahl, T. Heftrich, M. Heil, M. Heine, A. Heinz, A. Henriques, H. Hergert, A. Hufnagel, A. Ignatov, H. T. Johansson, B. Jonson, J. Kahlbow, N. Kalantar-Nayestanaki, R. Kanungo, A. Kelic-Heil, A. Knyazev, T. Kröll, N. Kurz, M. Labiche, C. Langer, T. Le Bleis, R. Lemmon, **S. Lindberg**, J. Machado, J. Marganiec, F. M. Marqués, A. Movsesyan, E. Nacher, M. Najafi, E. Nikolskii, T. Nilsson, C. Nociforo, S. Paschalis, A. Perea, M. Petri, S. Pietri, R. Plag, R. Reifarth, G. Ribeiro, C. Rigollet, M. Röder, D. Rossi, D. Savran, H. Scheit, A. Schwenk, H. Simon, I. Syndikus, J. T. Taylor, O. Tengblad, R. Thies, Y. Togano, P. Velho, V. Volkov, A. Wagner, H. Weick, C. Wheldon, G. Wilson, J. S. Winfield, P. Woods, D. Yakorev, M. Zhukov, A. Zilges, and K. Zuber, “Effective proton-neutron interaction near the drip line from unbound states in  $^{25,26}\text{F}$ ,” *Phys. Rev. C*, vol. 96, p. 054305, Nov 2017.

- IV.** M. Röder, T. Adachi, Y. Aksyutina, J. Alcantara, S. Altstadt, H. Alvarez-Pol, N. Ashwood, L. Atar, T. Aumann, V. Avdeichikov,



---

M. Barr, S. Beceiro, D. Bemmerer, J. Benlliure, C. Bertulani, K. Boretzky, M. J. G. Borge, G. Burgunder, M. Caamaño, C. Caesar, E. Casarejos, W. Catford, J. Cederkäll, S. Chakraborty, M. Chartier, L. Chulkov, D. Cortina-Gil, R. Crespo, U. Datta Pramanik, P. Diaz-Fernandez, I. Dillmann, Z. Elekes, J. Enders, O. Ershova, A. Estrade, F. Farinon, L. M. Fraile, M. Freer, M. Freudenberger, H. Fynbo, D. Galaviz, H. Geissel, R. Gernhäuser, K. Göbel, P. Golubev, D. Gonzalez Diaz, J. Hagdahl, T. Heftrich, M. Heil, M. Heine, A. Heinz, A. Henriques, M. Holl, G. Ickert, A. Ignatov, B. Jakobsson, H. Johansson, B. Jonson, N. Kalantar-Nayestanaki, R. Kanungo, A. Kelic-Heil, R. Knöbel, T. Kröll, R. Krücken, J. Kurcewicz, N. Kurz, M. Labiche, C. Langer, T. Le Bleis, R. Lemmon, O. Lepyoshkina, **S. Lindberg**, J. Machado, J. Marganec, M. Mostazo Caro, A. Movsesyan, M. A. Najafi, T. Nilsson, C. Nociforo, V. Panin, S. Paschalis, A. Perea, M. Petri, S. Pietri, R. Plag, A. Prochazka, M. A. Rahaman, G. Rastrepina, R. Reifarth, G. Ribeiro, M. V. Ricciardi, C. Rigollet, K. Riisager, D. Rossi, J. Sanchez del Rio Saez, D. Savran, H. Scheit, H. Simon, O. Sorlin, V. Stoica, B. Streicher, J. Taylor, O. Tengblad, S. Terashima, R. Thies, Y. Togano, E. Uberseder, J. Van de Walle, P. Velho, V. Volkov, A. Wagner, F. Wamers, H. Weick, M. Weigand, C. Wheldon, G. Wilson, C. Wimmer, J. S. Winfield, P. Woods, D. Yakorev, M. Zhukov, A. Zilges, and K. Zuber, “Coulomb dissociation of  $^{20,21}\text{N}$ ,” *Phys. Rev. C*, vol. 93, p. 065807, Jun 2016.

- V. M. Heine, S. Typel, M.-R. Wu, T. Adachi, Y. Aksyutina, J. Alcantara, S. Altstadt, H. Alvarez-Pol, N. Ashwood, L. Atar, T. Aumann, V. Avdeichikov, M. Barr, S. Beceiro-Novo, D. Bemmerer, J. Benlliure, C. A. Bertulani, K. Boretzky, M. J. G. Borge, G. Burgunder, M. Caamano, C. Caesar, E. Casarejos, W. Catford, J. Cederkäll, S. Chakraborty, M. Chartier, L. V. Chulkov, D. Cortina-Gil, R. Crespo, U. Datta Pramanik, P. Diaz Fernandez, I. Dillmann, Z. Elekes, J. Enders, O. Ershova, A. Estrade, F. Farinon, L. M. Fraile, M. Freer, M. Freudenberger, H. O. U. Fynbo, D. Galaviz, H. Geissel, R. Gernhäuser, K. Göbel, P. Golubev, D. Gonzalez Diaz, J. Hagdahl, T. Heftrich, M. Heil, A. Heinz, A. Henriques, M. Holl, G. Ickert, A. Ignatov, B. Jakobsson, H. T. Johansson, B. Jonson, N. Kalantar-Nayestanaki, R. Kanungo, A. Kelic-Heil, R. Knöbel, T. Kröll, R. Krücken, J. Kurcewicz, N. Kurz, M. Labiche, C. Langer, T. Le Bleis, R. Lemmon, O. Lepyoshkina, **S. Lindberg**, J. Machado, J. Marganec, G. Martínez-Pinedo, V. Maroussov, M. Mostazo, A. Movsesyan, A. Najafi, T. Neff, T. Nilsson, C. Nociforo, V. Panin, S. Paschalis, A. Perea, M. Petri, S. Pietri, R. Plag, A. Prochazka, A. Rahaman, G. Rastrepina, R. Reifarth, G. Ribeiro, M. V. Riccia-

---

rdi, C. Rigollet, K. Riisager, M. Röder, D. Rossi, J. Sanchez del Rio, D. Savran, H. Scheit, H. Simon, O. Sorlin, V. Stoica, B. Streicher, J. T. Taylor, O. Tengblad, S. Terashima, R. Thies, Y. Togano, E. Uberseder, J. Van de Walle, P. Velho, V. Volkov, A. Wagner, F. Wamers, H. Weick, M. Weigand, C. Wheldon, G. Wilson, C. Wimmer, J. S. Winfield, P. Woods, D. Yakorev, M. V. Zhukov, A. Zilges, and K. Zuber, “Determination of the neutron-capture rate of  $^{17}\text{C}$  for  $r$ -process nucleosynthesis,” *Phys. Rev. C*, vol. 95, p. 014613, Jan 2017.

# Contribution Report

## Contributions to Papers I, II, III, IV and V

I have contributed with developments of the program used for mass identification of the outgoing fragments. I have also made contributions to the add-back routine used in the Crystal Ball. These contributions were not only helpful for these papers but also for others and are also useful for future experiments. I have read and given suggestions for improvements of the manuscripts.

## Contributions to Paper I

As part of the development of the mass identification program, I developed a method to improve the virtual position alignment of the double-sided silicon strip detectors. This was necessary to be able to obtain the correct mass from all the different settings of the FRS used during the experiment. This method is also applicable for future experiments.

## Contributions to $^{29}\text{Ne}$ analysis

I participated in the preparation of the experiment by making NeuLAND operational after the transport to RIKEN from GSI. I also took part in the full experiment. I have calibrated all the detectors in the setup (F5, F7, SBT, BDC1, BDC2, MINOS, FDC1, FDC2, Hodoscope, NeuLAND and NEBULA) and analysed the data. I am writing a manuscript for a publication.



# Contents

<b>1</b>	<b>Introduction</b>	<b>1</b>
1.1	Nuclear Structure . . . . .	2
1.2	Nuclear Astrophysics . . . . .	5
1.3	Nuclear Physics Experiments . . . . .	7
<b>2</b>	<b>Experiments with Relativistic Radioactive Beams</b>	<b>9</b>
2.1	Invariant Mass . . . . .	9
2.2	Relative Energy . . . . .	10
2.3	Cross Sections . . . . .	11
2.4	Nuclear Reactions . . . . .	11
2.5	Experimental Facilities and Setups . . . . .	12
2.5.1	GSI/FAIR . . . . .	13
2.5.2	The R <sup>3</sup> B/LAND-setup . . . . .	14
2.5.3	RIKEN . . . . .	15
2.5.4	The SAMURAI-setup . . . . .	16
<b>3</b>	<b>Detector Calibrations</b>	<b>19</b>
3.1	Drift Chambers . . . . .	19
3.2	MINOS TPC . . . . .	23
3.3	DALI2 . . . . .	24
3.4	Hodoscope . . . . .	24
3.5	NeuLAND and NEBULA . . . . .	27
<b>4</b>	<b>Unbound states in <sup>29</sup>Ne</b>	<b>29</b>
4.1	Experiment . . . . .	30
4.2	Data Analysis . . . . .	30
4.3	Detector Efficiency and Acceptance . . . . .	33
4.4	Results and Discussion . . . . .	34
<b>5</b>	<b>Fragmentation Reaction Cross Sections of B and C Isotopes</b>	<b>43</b>
5.1	Experiment . . . . .	43
5.2	Data Analysis . . . . .	44
5.3	Results and Discussion . . . . .	44

<b>6</b>	<b>Unbound States in Be and F</b>	<b>47</b>
6.1	Data Analysis . . . . .	48
6.2	Results and Discussion . . . . .	49
<b>7</b>	<b>Coulomb Dissociation and Neutron Capture Rates</b>	<b>53</b>
7.1	Data Analysis . . . . .	53
7.2	Results and Discussion . . . . .	54
<b>8</b>	<b>Summary</b>	<b>57</b>
	<b>Bibliography</b>	<b>59</b>

# Chapter 1

## Introduction

The matter around us consists of atoms. The existence of stable atoms is crucial for the existence of the world as we know it, and the stability of atoms is governed by the stability of their nuclei, consisting of protons and neutrons. How nuclei are bound together, and why certain nuclei are stable and others not, are questions which cannot be answered fully satisfactory yet. The nature of nuclei is also important for understanding the origin of the visible matter around us. All elements have been created in nuclear reactions in different astronomical objects and phenomena, such as stars, supernovae, and neutron star mergers. To understand these astrophysical processes, many answers can be found in nuclear physics.

The atomic nucleus constitutes a complex quantum mechanical many-body system consisting of nucleons; protons and neutrons. Inside the nucleus they all interact with each other via the nucleon-nucleon interaction, which is a residue of the strong force acting between quarks in the nucleons. This makes the atomic nuclei the largest system governed by the strong interaction. The nucleon-nucleon interaction is strongly repulsive for distances between nucleons which are shorter than about 0.5 fm. For longer distances it is attractive and has its maximum at around 1 fm, while for distances larger than a few fm it becomes negligible. Since protons are electrically charged, also the electromagnetic interaction plays a role. To create a bound nucleus, the repulsive force between the protons has to be overcome by the nucleon-nucleon interaction.

If the mass of the nucleus is less than the sum of the individual nucleon masses, it forms a bound system where the excess mass is stored as binding energy. If a nucleus is bound or not depends on the number of nucleons ( $A$ ), the ratio between neutrons ( $N$ ) and protons ( $Z$ ), and the internal structure of the nucleus. Even if a nucleus is bound, it is not necessarily stable. A nucleus can, e.g.  $\beta$ -decay via the weak interaction, changing one proton into a neutron or vice versa. This may happen if the binding energy is increased by the process, otherwise the nucleus is stable against  $\beta$ -decay. These nuclei

are said to be situated in the so-called valley of  $\beta$ -stability. For lighter nuclei,  $A < 50$ , this runs close the line where  $N = Z$ . For heavier nuclei this line bends towards nuclei with  $N > Z$ .

Several models have been developed to describe the properties of atomic nuclei. So far none has been able to reproduce the correct properties for all of the over 3000 isotopes, which have been observed so far. Instead, different models are successful in different parts of the nuclear chart. Among the first models developed were the liquid drop model and the nuclear shell model [1, 2] which is still widely used today. It also plays a key role in the work of this thesis.

To be able to develop improved and more general models, it is essential to get a better understanding of the nucleon-nucleon interaction. Properties of exotic nuclei, consisting of many more protons than neutrons or vice versa, may be more sensitive to normally small effects in the nucleon-nucleon interaction in stable nuclei. Hence, exotic nuclei are useful to learn more about the interactions between the nucleons as the otherwise small details may be easier to extract.

In this thesis, results from different experiments using beams of exotic nuclei are presented. The nuclei, which are treated in this thesis, are marked in pink in the chart of nuclides in Fig. 1.1. The results cover unbound states in  $^{29}\text{Ne}$ ,  $^{13}\text{Be}$  and  $^{26}\text{F}$ , presented in Ch. 4 and 6 and Papers II and III. In Paper I, the fragmentation cross sections for several carbon and boron isotopes are measured and in Papers IV and V, the Coulomb dissociation cross sections of  $^{20,21}\text{N}$  and  $^{18}\text{C}$  are reported and used to calculate the neutron capture cross sections for  $^{19,20}\text{N}$  and  $^{17}\text{C}$  important in models describing the r-process nucleosynthesis.

### 1.1 Nuclear Structure

One of the models which is still widely used is the nuclear shell model [1, 2]. Due to the Pauli exclusion principle, each shell, comprised of one or several single-particle orbitals, can only hold a limited number of nucleons. The shell model was developed based on the experimental data showing much higher binding energies for nuclei with 2, 8, 20, 28, 50, 82, 126 or 184 nucleons compared to when another nucleon was added or removed. These are called the *magic numbers*, and correspond to completely filled shells, either proton or neutron shells. If both, the neutron and proton shells are completely filled, the nucleus is said to be doubly magic.

The energy levels are given by solving the Schrödinger equation with an appropriate potential. The Woods-Saxon potential is widely used for this purpose and is similar to the harmonic oscillator potential, but has a flatter bottom and a steeper rise. A similar shape of the potential can be achieved also with the harmonic oscillator by adding an  $l^2$  term, where  $l$



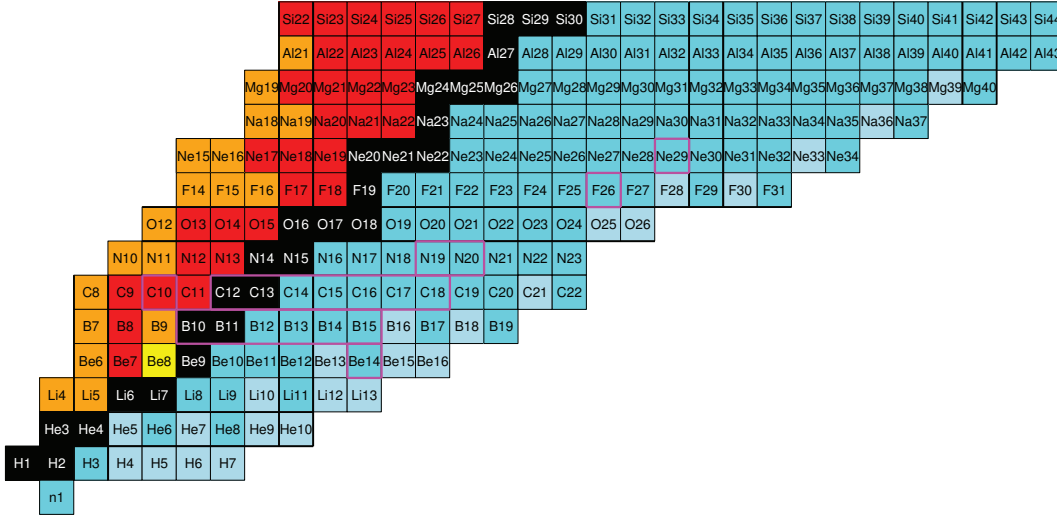


**Figure 1.1:** The chart of the nuclides for the lightest isotopes. The traditional magic numbers are marked with thick black lines and the nuclei marked with pink are the ones which are discussed in this thesis. The colours denote the type of decay, orange for proton emission, red for  $\beta^+$ -decay, or electron capture, yellow for  $\alpha$ -decay, blue for  $\beta^-$ -decay, light blue for neutron emission and black for stable isotopes.

is the orbital angular momentum of a nucleon. The shape of the potential is due to the nature of the nucleon-nucleon interaction, which has a short range. Because of the short range, the potential experienced by a nucleon is, mostly, created by its closest neighbours. Nucleons in the centre of the nucleus are surrounded by other nucleons, hence all nucleons in the centre experience the same potential as they have approximately the same number of neighbouring nucleons. The nucleons at the surface of the nucleus though, have fewer neighbouring nucleons and hence experience a weaker potential. As a consequence, the Woods-Saxon potential is rather constant close to the centre of the nucleus but has a steep rise when approaching the surface.

Using only the Woods-Saxon potential to solve the Schrödinger equation, the magic numbers do not agree with experimental data, though. To solve this, Mayer and Jensen [1, 2] suggested to add a spin-orbit coupling term to the potential. The addition of spin-orbit coupling leads to a splitting of the degenerate orbits as shown in Fig. 1.2. After the splitting new energy gaps occur at 28 and 50, while the gap at 40 disappears, which agrees well with experimental data. The ordering and distances between the different single particle states are not constant though. This is caused by the widening of the potential with the number of nucleons in the nucleus, decreasing the energy for the single particle states with increasing number of nucleons. A larger effect is the residual interaction between nucleons in closed shells and valence nucleons which can affect the energy of single particle states

greatly [3].

The picture in the shell model where each nucleon is occupying a specific single-particle state is a simplification. Quantum mechanically, the nucleons can occupy several different single-particle states with a given probability. As the nucleon can occupy several different orbitals, its total wave function is a super-position of all the different possible single-particle configurations. This is called configuration mixing. Already for quite simple nuclei, with just a few valence nucleons, the calculations become very complicated as there is in general a very large number of single-particle configurations which can contribute. This becomes even worse when taking into account possible particle-hole excitations from closed shells.

When exciting a nucleus above the nucleon emission threshold energy, the system becomes unbound. This is the case for both  $^{29}\text{Ne}$  and  $^{26}\text{F}$ , studied in this thesis. For  $^{13}\text{Be}$  the energy threshold is below the ground state energy though, and hence it is an unbound nucleus. The unbound states of these nuclei close to the neutron dripline are very interesting for understanding the transition from bound nuclei to the continuum. They also provide clues to better understand the shell evolution in nuclei.

A closed-shell nucleus has a spherical shape. When several nucleons are removed or added, the shape of the nucleus can take an oblate or prolate shape. A measure of the deformation of a nucleus is its nonzero electric quadrupole moment. With non-spherical nuclear shapes new types of excitations are possible, namely collective rotational excitations, in addition to collective vibrations near closed shells. It is not only possible to have deformed nuclei, but the nucleons can also be separated spatially within the nucleus creating so-called halo nuclei. This phenomenon was first observed

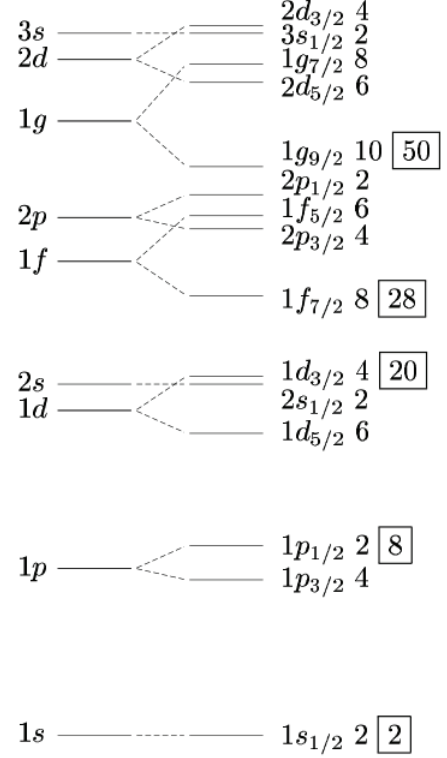


**Figure 1.2:** The ordering of the lowest-lying energy states in the nuclear shell model. The magic numbers are shown in the squares to the right where the shell gaps occur. This figure is valid for nuclei close to the valley of stability, for more exotic nuclei the ordering of the orbitals can change as well as the magic numbers.

in  $^{11}\text{Li}$  [4, 5], which consists of a  $^9\text{Li}$  core with a 2-neutron halo, where the two neutrons are at a much larger distance from the rest of the nucleons in the  $^9\text{Li}$  core. The root-mean-square matter radius of  $^{11}\text{Li}$  is comparable to  $^{48}\text{Ca}$  and the radius of the halo is about the same size as a  $^{208}\text{Pb}$  nucleus [6]. After the discovery of the  $^{11}\text{Li}$  halo structure, several such nuclei have been found. The heaviest observed halo nuclei so far are  $^{29,31}\text{Ne}$  [7, 8] and  $^{37}\text{Mg}$  [9]. These are all 1-neutron halo nuclei and the  $^{29}\text{Ne}$  isotope is discussed in Ch. 4.

The isotope  $^{29}\text{Ne}$  is not only interesting because it is a halo nucleus, it is also situated in a very interesting region of the nuclear chart, the island of inversion. In this region, the shell closure at  $N=20$  disappears. This has been suggested to be caused by intruder states from the  $fp$ -shells [10, 11] which also may lead to shape coexistence [12, 13]. The intruder states are caused by the  $1d_{3/2}$  and  $1f_{7/2}$  states moving closer to each other, compared to in Fig. 1.2, and as a consequence the shell gap at  $N=20$  disappears. Why these states move closer to each other is still an open question. Hence it is important to find out more about the structure of the nuclei in this area, to understand what processes drive the states closer together in comparison with model calculations. Also the unbound  $^{13}\text{Be}$  exists in a region where the shell closure disappears. In this case the  $N=8$  shell closure has been observed to break down for  $^{12}\text{Be}$  [14].

## 1.2 Nuclear Astrophysics

The creation of baryonic matter is one of the big questions within nuclear astrophysics. We know that during the Big Bang only hydrogen, helium and small amounts of lithium and beryllium were created [15–17]. After the Big Bang, the formation of stars and galaxies began. In the stars, stellar nucleosynthesis takes place which can create new elements up to nickel and iron [18]. To create heavier elements, other nucleosynthesis processes are needed. The creation of about half of the heavier elements can be explained, mostly, by slow neutron capture, the s-process, and photodisintegration, the p-process [19]. The remaining isotopes found in nature are created in the rapid neutron capture process, the r-process. The s-process takes place in low-mass asymptotic giant branch stars and during the He and C burning phases of massive stars [20]. During the s-process, free neutrons are captured at a low rate. Because the capture rate is low,  $\beta$ -unstable isotopes decay before capturing another neutron. Hence, the s-process runs close to the valley of  $\beta$ -stability. The p-process takes place in massive stars and supernovae [21]. The basic principle of the process is that it starts with heavy elements created by s- and r-processes. By photodisintegrations, mainly neutrons, protons and alphas are emitted from the nucleus, and new elements are created. By consecutive photodisintegration reactions and

subsequent decays, a group of stable isotopes are populated along the proton-rich side of the valley of stability.

The r-process is similar to the s-process in the sense that nuclei capture neutrons. But in contrast to the s-process,  $(n,\gamma)$  reactions occur at a very high rate, which does not allow  $\beta$ -decay before a new neutron is captured. This creates very neutron-rich nuclei, but the more neutrons are added to a nucleus, the shorter the  $\beta$ -decay half-lives become. Eventually the lifetime of the nucleus is comparable to the neutron capture rate. Those nuclei are called waiting-point nuclei. As the nucleus  $\beta$ -decays it moves up the nuclear chart. If the daughter nucleus has a longer lifetime, it is likely to capture further neutrons. In this way neutron-rich nuclei are created far from the valley of stability. That the process depends on the properties of very short-lived nuclei is one of the reasons it is less understood than the s- or p-processes. Because of their short lifetimes, they are much harder to study than stable nuclei, and many of their properties uncertain. This leads to uncertainties in the reaction network models of the r-process, especially since small deviations early in the reaction chain can result in large fluctuations later. The capture rate for three C and N isotopes are measured in Paper IV and V.

In which astrophysical scenario the r-process takes place has been an open question for decades. Two of the most common suggestions have been core-collapse supernovae and neutron star mergers. Very recently, in 2017, strong evidence was found that the r-process takes place in neutron star mergers, though. This observation was a major break-through as the astronomical event was detected by several different measurements, both gravitational waves and electromagnetic radiation. The first observation of the merger was made by the VIRGO and LIGO detectors measuring gravitational waves. Less than two seconds after the merge a  $\gamma$ -ray burst was detected. This was followed by observations of a bright optical transient about 11 hours after the merge by several different groups. The continued observations showed a redward evolution of the optical and infrared light during 10 days. X-rays and radio emissions were not observed until 9 and 16 days after the merge, respectively. These observations led to the conclusion that a neutron star merger had been observed followed by a kilonova in which the r-process took place [22, 23].

There are still many open questions concerning both the r-process and its exact properties, such as its path. Moreover, it has been suggested that there exists an intermediate neutron capture process, i-process [24]. For this process, a higher neutron flux is needed than for the s-process but it is not as high as that for the r-process. These circumstances may be achieved in red giants undergoing helium shell flashes. However, like the r-process this model also suffers from the uncertain properties of the isotopes involved in the process [25]. To improve the models, especially the neutron capture cross sections need to be measured for the isotopes involved.

## 1.3 Nuclear Physics Experiments

To study unstable isotopes they have to be measured within at most a few half-lives. For very short-lived nuclei, this creates a large experimental challenge. Furthermore, it is not sufficient to just create the isotope of interest, one also wants to probe its properties. One way of doing this is to study its interaction with other nuclei. This can be achieved by using the in-flight method where a beam of heavy ions is accelerated and impinges on a light target. By fragmentation and fission reactions, short-lived isotopes are created which can be transmitted to the experimental setup.

The in-flight method is well-suited for experiments with short-lived nuclei. They are produced by accelerating stable ions, to velocities ranging from a few ten up to about 90 percents of the speed of light, and then collide them with a target. At those energies, fragmentation and fission reactions create a wide range of mostly unstable isotopes. From the produced ions the ones of interest have to be separated from the rest. This is achieved by the use of magnetic fields, slits and energy degraders. This is the method employed in the experiments presented in this thesis. In Ch. 2 a more detailed description of the two acceleration facilities and experimental setups is given.

The advantage of the in-flight method is that no post-acceleration is needed and that the ions are leaving the target due to their high kinetic energy. This makes it possible to study very short-lived nuclei which are travelling at relativistic velocities as they are directed to the experimental setup directly after creation. Experiments are limited by the time it takes to transport it to the experimental setup, usually a few hundred nanoseconds. This short transmission time may cause problems though, as isomeric states can be populated. On the other hand, this can also be exploited to study isomeric states. Another problem, mainly for heavy ions, is that they may not be fully stripped of electrons, which complicates the beam identification. Here higher beam energies increase the fraction of fully-stripped ions.

In contrast to more classical nuclear physics experiments, in-flight experiments are performed in inverse kinematics. This means that the nuclei of interest are the projectiles scattering off the typically lighter nuclei in the target. The main reason for this approach is that it is simply not possible to create a target of very unstable nuclei. Even though this is a necessity for studying the very short-lived isotopes, the method also has other advantages compared to the direct kinematics approach: For sufficiently high beam energies and small enough target thickness, the nucleus of interest leaves the target. This simplifies the identification of reaction products, which in turn makes it easier to reconstruct the reaction event-by-event.

Another advantage of this experimental method is that the reaction products are very forward focused due to the relativistic kinematics. Hence, the full solid angle in the center-of-mass frame of the reaction, can be covered

## 1. Introduction

---

by detectors only in the forward direction in the lab. The only exception is the detection of  $\gamma$ -rays, which profits from covering also larger angles.

## Chapter 2

# Experiments with Relativistic Radioactive Beams

The basic concept of a radioactive beam experiment is that a stable beam is accelerated and impinges on a production target. In the resulting nuclear collisions, radioactive nuclei are produced, together with stable isotopes, and a radioactive secondary beam is extracted from the reaction products [26]. This secondary beam is then transmitted to the experimental setup, where it impinges on a second target. This allows to investigate the radioactive nuclei by measuring reaction cross sections, producing even more exotic nuclei or populating unbound states [27].

The detectors in the experimental setup typically measure quantities such as energy deposited, times and hit positions. By combining the information from the detectors, properties of the nuclei can be reconstructed, e.g. charges, masses and momenta. These quantities can then be used to reconstruct more complicated nuclear properties. In this work I will refer to the reconstructed quantities as observables. The most important observables for this work are the invariant mass, the relative energy and cross sections, which are described in more detail in the following sections.

### 2.1 Invariant Mass

The invariant mass is a quantity which is Lorentz-invariant, i.e. it is constant in all inertial frames. The invariant mass is defined by the square of the 4-momentum of a particle. Using natural units, with  $c=1$ , the equation can be written as

$$M_i^2 = P^2 = E^2 - \vec{p}^2 \quad (2.1)$$

where  $M_i$  is the invariant mass,  $\mathbf{P}$  is the 4-momentum,  $E$  is the energy and  $\vec{p}$  is the 3-momentum.

## 2.2 Relative Energy

In the case of an unbound system, such as an unbound nucleus or a nucleus excited above the particle-emission threshold, the relative energy provides information about the energy of the system before particle emission. This can be used to extract excitation energies as well as information about the nature of these states. The relative energy is calculated as the difference of the invariant masses before and after the emission. In the case of a one particle emission, the invariant mass can be written as

$$M_{\text{fn}} = \sqrt{(\mathbf{P}_f + \mathbf{P}_n)^2} = \sqrt{(E_f + E_n)^2 - (\vec{p}_f + \vec{p}_n)^2}, \quad (2.2)$$

where  $M_{\text{fn}}$  is the invariant mass of the fragment plus the emitted nucleon,  $\mathbf{P}$  is the 4-momentum,  $E$  the energy and  $\vec{p}$  the 3-momentum. Indices f and n denote the fragment and the nucleon, respectively. Using  $E^2 - \vec{p}^2 = m_0^2$ , where  $p$  is the total momentum and  $m_0$  the rest mass, the invariant mass can be written as

$$M_{\text{fn}} = \sqrt{M_f^2 + M_n^2 + 2E_f E_n - 2p_{fx}p_{nx} - 2p_{fy}p_{ny} - 2p_{fz}p_{nz}}, \quad (2.3)$$

with  $M_f$  and  $M_n$  denoting the rest masses of the fragment and the emitted nucleon, and  $p_{fx}$  and  $p_{nx}$  denoting the momenta in the  $x$ -direction of the fragment and the emitted nucleon, respectively. Since  $E = m_0\gamma$  and  $p = m_0\gamma\beta$ , with  $\gamma$  being the Lorentz factor and  $\beta$  the velocity in units of  $c$ , this can be further simplified to

$$M_{\text{fn}} = \sqrt{M_f^2 + M_n^2 + 2M_f M_n \gamma_f \gamma_n (1 - \beta_f \beta_n \cos \theta_{\text{fn}})}, \quad (2.4)$$

where  $\theta_{\text{fn}}$  is the angle between the momentum vectors of the fragment and the emitted nucleon. As the relative energy is given by the difference of the invariant mass before and after the reaction, the initial mass has to be subtracted and the equation for the relative energy is written as

$$E_{\text{fn}} = \sqrt{M_f^2 + M_n^2 + 2M_f M_n \gamma_f \gamma_n (1 - \beta_f \beta_n \cos \theta_{\text{fn}})} - M_0, \quad (2.5)$$

where  $M_0$  is the mass of the initial system. For unbound systems,  $M_0$  is the same as the sum of the rest masses of the fragment and the emitted nucleon. However, when the nucleon is emitted, the daughter nucleus may not be in its ground state, but in a bound excited state from which it decays by  $\gamma$ -emission, which has to be considered when calculating the total excitation energy.



## 2.3 Cross Sections

Cross sections, denoted  $\sigma$ , are a measure of how likely a nuclear reaction is to occur. It is given in units of barns (b) where  $1 \text{ b} = 10^{-24} \text{ cm}^2$ . Cross sections are calculated, for a thin target, by dividing the number of ions that reacted,  $N_r$ , with the total number of incoming ions,  $N_i$ , and the number of nuclei in the target per area,  $N_{t,\text{cm}^{-2}}$ ,

$$\sigma = \frac{N_r}{N_i \cdot N_{t,\text{cm}^{-2}}}. \quad (2.6)$$

Cross sections are of importance when designing experiments, to estimate how many reactions will occur and hence how much statistics can be expected. In Paper I the proton removal cross sections are measured for different boron and carbon isotopes. Cross sections can also be used to obtain information on nuclear structure, see e.g. [28, 29]. Cross sections are also important for models describing nucleosynthesis, e.g. the neutron capture cross section is very important for modelling of r-process nucleosynthesis, discussed in Papers IV and V. Historically, it was the much enhanced total interaction cross section of  ${}^{11}\text{Li}$  that led to the discovery of halo nuclei [4].

## 2.4 Nuclear Reactions

The aim of an experiment is usually to study one or more specific quantum states of a nucleus. To populate a specific state of interest in our case, a nuclear reaction has to occur at the secondary target. To maximise the probability of populating the state of interest, essentially three parameters affecting the nuclear reaction can be tuned. These parameters are the beam energy and ion species as well as the target material. There is one key parameter of the reaction which cannot be affected, namely the impact parameter. This parameter measures the perpendicular distance of the projectile trajectory from a central head-on collision, and defines how much the effective areas of the projectile and target nuclei overlap. For this work, the most important reactions are projectile fragmentation and knockout reactions.

Fragmentation reactions are primarily used to create the radioactive beam which is described in Sec. 2.5.1 and 2.5.3. In a fragmentation reaction only a part of the incoming projectile is interacting with a part of the target nucleus. At impact, nucleons in the overlap zone scatter and they may in turn interact with other nucleons, mostly in that zone, creating an intra-nucleon cascade where a large part of the nucleons in both the target and projectile nuclei are knocked out of their respective nuclei. In a more simplified picture this can be seen as the part of the target nucleus overlapping with the projectile nucleus is removed [30]. This means that the impact parameter together with the relative size of the nuclei are decisive

for how much of the projectile nucleus is removed. After the fragmentation reaction, the so-called pre-fragment is typically in a highly excited state. This state decays according to the statistical model via particle evaporation and  $\gamma$ -emission. As already mentioned, fragmentation reactions are used for the production of radioactive beams, but can also be used for studying the created fragment via  $\gamma$ -ray spectroscopy.

Knockout reactions are in some sense similar to fragmentation reactions, but with the major difference that in this case only two nucleons are involved in the reaction. One nucleon in the projectile is knocked out when scattered against a nucleon in the target nucleus. The big advantage of this kind of reactions is that since the interaction only takes place between two nucleons, the rest of the nucleus is left unchanged. By studying the transversal or parallel momentum of the remaining fragment, information about the knocked out nucleon can be obtained. It can also be used to study excited states via  $\gamma$ -spectroscopy, or unbound states by measuring the relative energy described in Sec. 2.2. A special case of knockout reactions is quasi-free scattering.

To maximise the probability of knocking out a deeply bound nucleon, a small target nucleus, preferably protons, should be used. Also the beam energy should be set so that the nucleon-nucleon interaction cross section is as small as possible. This has two reasons, it increases the probability of the proton penetrating into the projectile nucleus, and it improves the probability of the proton and knocked out nucleon to get out of the nucleus without interacting with the other nucleons. The optimal energy depends on whether the wanted interaction is a p-p or p-n reaction. For proton knockout, the best energy is in the interval 200 – 2000 MeV/nucleon, while for neutron knockout the energy should be above 700 MeV/nucleon [31].

### 2.5 Experimental Facilities and Setups

For a long time nuclear physics was limited to experiments with beams of stable, or at least long-lived isotopes. This changed with the advent of radioactive beam facilities, opening up new possibilities to study very short-lived isotopes. There exists a few of these facilities in the world today, and among the biggest are GSI/FAIR in Germany, RIKEN in Japan and FRIB in the United States. In this thesis I present results from GSI/FAIR and RIKEN. The main difference between them is that at GSI/FAIR radioactive beam production is based on a synchrotron accelerator, while RIKEN uses cyclotrons. A cyclotron does not change its magnetic field during acceleration, instead the beam trajectory has the shape of a spiral and this can deliver a higher integrated beam intensity. When the ions are accelerated their magnetic rigidity increases and they are bent less in the magnetic field, thus moving outwards in the spiral. The limitation of the maximum energy

delivered from a cyclotron is given by its size and maximum magnetic field. To not have to build bigger and bigger cyclotrons, an alternative is a synchrotron accelerator. This type of accelerator has a fixed radius and instead the magnetic field is changed as the ions are accelerated. For both cyclotron and synchrotron facilities the initial acceleration may be done in a linear accelerator.

### 2.5.1 GSI/FAIR

The beams at GSI/FAIR are created using different types of ion sources including MUCIS (MULTi Cusp Ion Source), PIG (Penning ion gauge), CHORDIS (Cold or HOT Reflex Discharge Ion Source), VARIS (Vacuum ARc Ion Source) and MEVVA (MEtal Vapor Vacuum Arc Ion Source) [32]. Which source is used depends on what beam is needed. The MUCIS and CHORDIS only works with gaseous elements such as  $H_2$ ,  $N_2$ , Ne or Xe, while the other sources also can use solid materials such as Mg, Ti and Au. The heaviest ions which can be accelerated at GSI are uranium ions which are extracted from VARIS. The ions extracted from the source are stable<sup>1</sup> and accelerated in the linear accelerator UNILAC. In the linear accelerator the ions are accelerated up to around 10 MeV/nucleon before they are injected into the ring accelerator SIS18, which is a synchrotron accelerator with a circumference of 216 m, able to accelerate ions up to 1–4.5 GeV/nucleon<sup>2</sup>, equivalent to about 90% of the speed of light. When the beam has been accelerated to the desired energy, it is directed to the fragment separator FRS [33]. A schematic drawing of the FRS is shown in Fig. 2.1. At the beginning of FRS the beam collides with a production target, typically consisting of beryllium due to its relatively high density and heat resistance. When the ions in the beam collide with nuclei in the target, a wide range of different isotopes are created. This is due to projectile fragmentation and knockout reactions<sup>3</sup>. For downstream experiments to have only the ions of interest in the beam, these need to be separated from all other ions created.

The separation is done using the  $B\rho - \Delta E - B\rho$  method [33,34]. In the first step the beam is deflected using dipole magnets. Depending on the magnetic rigidity,  $B\rho$ , the ions are bent differently. The magnetic rigidity is given by the ratio of momentum  $p$  and charge  $q$  of the ion. Assuming that the ion is fully stripped, the charge is given by the number of protons  $Z$  times the elementary charge  $e$ . The momentum is given by the equation  $p = m\gamma\beta c$  where  $m$  is the mass,  $\gamma$  the Lorentz factor, and  $\beta c$  the velocity.

---

<sup>1</sup>U is not stable but has a very long half-life ( $4.5 \cdot 10^9$  years for  $^{238}\text{U}$ ).

<sup>2</sup>The maximum energy depends on what ions are being accelerated, for U the maximum energy is 1 GeV/nucleon and for protons it is 4.5 GeV.

<sup>3</sup>For heavier isotopes also in-flight fission reactions can occur.

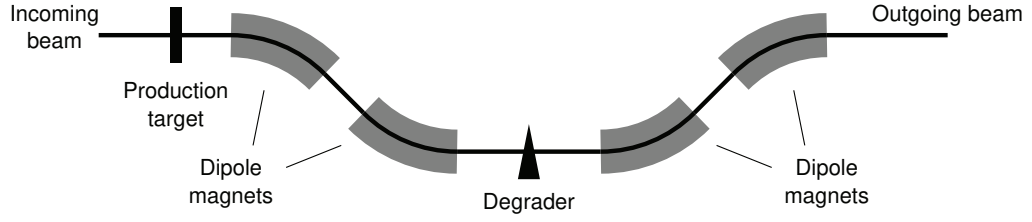


**Figure 2.1:** Schematic drawing of the FRS. The incoming stable beam impinges on the production target. With the dipole magnets and the degrader a selection of which ions should be transmitted to experiments is made, based on the charge, mass and momentum of the ions.

This gives the following equation for the magnetic rigidity

$$B\rho = \frac{p}{q} = \frac{m\gamma\beta c}{Ze}. \quad (2.7)$$

Since the ions in the beam all travel at approximately the same velocity,  $\beta$ , a selection on the mass-over-charge ratio can be made. In practice this is done by slits which block ions too far from the central beam trajectory. In the next step a wedge-shaped degrader is used. When the ions pass the degrader they lose energy, which is proportional to the square of the fragment charge, hence the outgoing velocity is different for different charges. According to Eq. (2.7) also the magnetic rigidity depends on the velocity and thus a second selection on the magnetic rigidity can be done. This selection is done in the same way as in the first step using dipole magnets and slits. The beam is finally sent to the experimental setup, in the cases reported here, the R<sup>3</sup>B/LAND-setup.

### 2.5.2 The R<sup>3</sup>B/LAND-setup

The R<sup>3</sup>B/LAND-setup, which is shown in Fig. 2.2, is used to perform kinematically complete measurements, meaning that all incoming as well as outgoing reaction fragments are identified and their 4-vectors are measured. To achieve this, many different detectors are needed. The incoming ions first impinge on a thin plastic scintillator detector (POS) used for time-of-flight (ToF) measurements. It is also able to measure the energy loss as well as the hit position using 4 photo-multiplier-tubes (PMTs). After this an active veto detector (ROLU) is used to set the beam size. This detector consists of four movable plastic scintillators with a gap in between them where the beam can pass. If an ion hits any of the scintillators the event is discarded. A position sensitive PIN-diode (PSP) detector is used for position information. Before the beam impinges on the secondary target it passes two double-sided silicon strip detectors (SSTs) used for tracking the beam.

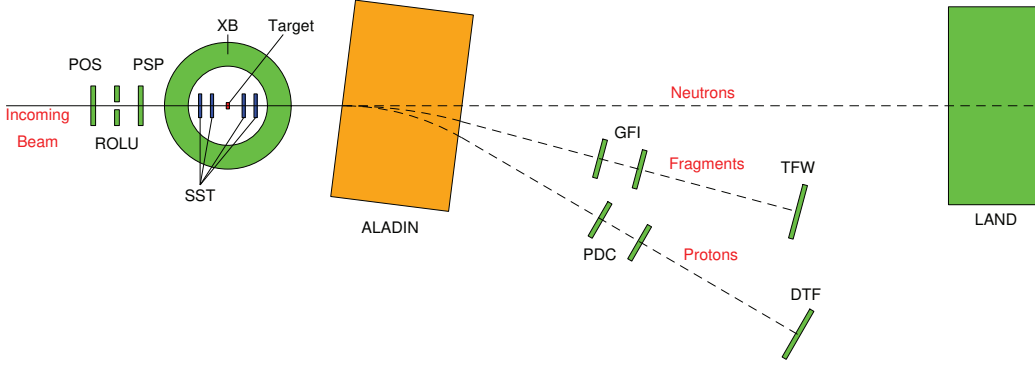


**Figure 2.2:** A schematic view of the R<sup>3</sup>B/LAND-setup. The incoming ions and outgoing fragments as well as other reaction products are identified and measured event-by-event. For details, see text.

Surrounding the target is the crystal ball [35] (XB) which detects  $\gamma$ -rays and protons scattered at large angles. Behind the target are two more SSTs for tracking the outgoing fragment. The fragments and protons are deflected in the large acceptance dipole magnet (ALADIN). Downstream from ALADIN the fragments are tracked using position measurements of two fiber detectors [36] (GFI) and the ToF is measured using a stop signal from the time-of-flight wall (TFW). The TFW also measures the energy loss for charge identification of the fragment. In a similar fashion, the protons are tracked in two drift chambers (PDC) and the ToF is measured using the DTF. Neutrons are not affected by the magnetic field and end up in the neutron detector (LAND) [37] which measures the ToF and the hit position.

### 2.5.3 RIKEN

The ions at the RIKEN Nishina Center for Accelerator-Based Science, shown in Fig. 2.3, are extracted from an electron cyclotron resonance ion source and initially accelerated with a linear accelerator. In the linear accelerator the ions are accelerated to a few MeV/nucleon. The beam is then further accelerated in four coupled cyclotrons. The first is a K540<sup>4</sup> ring cyclotron called RRC. It is able to accelerate the ions up to 63 MeV/nucleon. After this the beam is sent to a K570 ring cyclotron, the fRC. Unlike the other cyclotrons at RIKEN this is a fixed frequency machine. The third cyclotron is the 980K, IRC, which is able to accelerate the beam up to 127 MeV/nucleon. The final accelerator is the K2600 SRC. This is a superconducting cyclotron operating at 4.5 K creating a maximum magnetic field of 3.8 T. The maximum energy delivered from the SRC is 345 MeV/nucleon [38].

<sup>4</sup>The K-value of a cyclotron defines the kinetic energy reach of protons from the bending strength in a non-relativistic approximation.

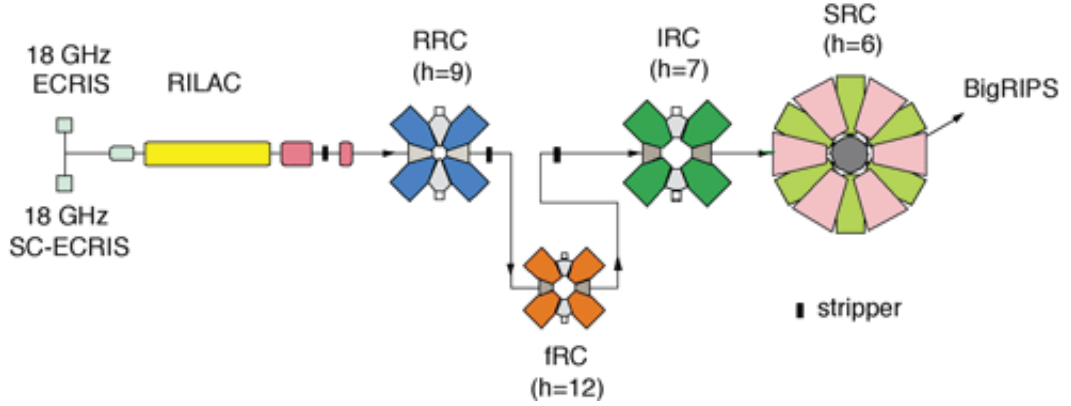


**Figure 2.3:** An overview of the accelerators at RIKEN. The ions are extracted from the electron cyclotron resonators (ECRIS). The beam is then accelerated, first in the linear accelerator (RILAC), then the cyclotrons (RRC, IRC and IRC) and finally in the superconducting cyclotron (SRC), in the end reaching energies up to 345 MeV/nucleon.

The beam from the SRC is directed to the BigRIPS fragment separator [39]. The beam impinges on a production target creating a wide range of different isotopes by projectile fragmentation. The selection of the desired isotope(s) is done using the  $B\rho - \Delta E - B\rho$  method, as in the FRS. The produced radioactive beam is then sent to the experimental setup. For the measurements of unbound states in  $^{29}\text{Ne}$ , the SAMURAI setup was used.

#### 2.5.4 The SAMURAI-setup

There are many similarities between the SAMURAI-setup [40] and the R<sup>3</sup>B/LAND-setup. The basic principle is the same: identify and measure the 4-vectors of all incoming and outgoing reaction products. A schematic view of the SAMURAI-setup is shown in Fig. 2.4. The identification of the incoming ions is made with the SBT-detector which consists of two thin plastic scintillators. They measure the ToF from BigRIPS and the energy loss. After this two tracking detectors, BDC1 and BDC2 are mounted. These are identical multi-wire drift chamber detectors. The chambers are filled with isobutane ( $\text{C}_4\text{H}_{10}$ ) kept at about 100 torr. Each drift chamber consists of 8 layers of wires with a separation of 4.8 mm and each layer has 16 wires separated by 2.5 mm. Every second wire acts as anode and the other as cathodes. By applying a voltage, an electric field is created between the anodes and cathodes. When an ion passes through the chamber it ionizes the gas atoms in the chamber. Due to the electric field the released electrons drift towards the anodes. The measurement of the drift time makes it possible to calculate how far from the wire the ion passed. When this is done for all planes in the detector, the ion can be tracked. This information is used



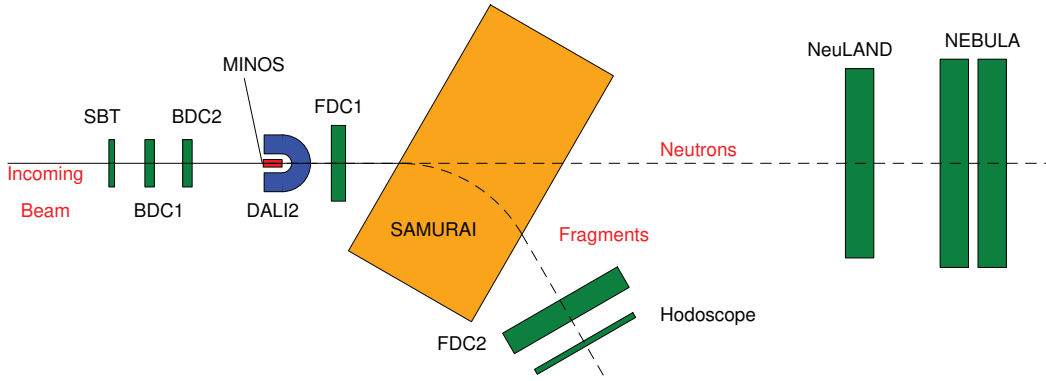


**Figure 2.4:** A schematic view of the SAMURAI-setup. For details, see the text.

to calculate the hit position at the MINOS target. MINOS consists of liquid hydrogen contained in a cylinder with radius 19 mm and a length of 150 mm. To obtain the vertex position the target chamber is surrounded by a time projection chamber (TPC). The principle of this detector is similar to that of the drift chambers. When an ion passes through the TPC it ionizes the gas along its track. In the chamber an electric field is applied which makes the electrons drift towards the back-end of the chamber. At the end of the chamber a layer of micromegas detectors are placed. These give the x and y-position of the ion, while the measured drift time is used to calculate the z-direction of the track.

The target is surrounded by the  $\gamma$  detector DALI2 [41]. It consists of 142 NaI(Tl) crystals providing both time and energy information. The crystals come in three different sizes,  $45 \times 80 \times 160 \text{ mm}^3$ ,  $40 \times 80 \times 160 \text{ mm}^3$  and  $60 \times 60 \times 160 \text{ mm}^3$ , and all are read out with photomultiplier tubes. Behind the target is another multi-wire drift chamber (FDC1) for tracking the outgoing fragments. It is similar to BDC1 and 2 but consists of 14 layers with wires, each with 32 wires separated by 5 mm. The layers are oriented in three different ways, either vertical or rotated clockwise or anti-clockwise 30 degrees around the vertical axis. This gives a good resolution in the x-direction, but still makes it possible to determine the y-position. When the fragments reach the large dipole magnet (SAMURAI), they are deflected due to the magnetic field and subsequently pass another drift chamber (FDC2). This detector is very similar to FDC1, in principle the only difference is the size. It has also 14 layers but each layer consists of 224 wires 10 mm apart. The final detector the fragments hit is the hodoscope. It consists of 24 plastic scintillator bars used to measure the ToF as well as the energy loss. The combination of the energy loss, ToF and the track makes it possible to identify and calculate the 4-vectors of the outgoing fragments.

Neutrons created in the reactions at the target are not affected by the

magnetic field in SAMURAI and thus reach the neutron detectors NeuLAND and NEBULA. They both consist of plastic scintillators, but since the neutrons are not electrically charged, they cannot be directly detected. Instead they have to interact with the nuclei in the detector creating charged particles with kinetic energy which in turn create scintillating light in the detectors.

NeuLAND consists of 8 layers of  $50 \times 50 \times 2500 \text{ mm}^3$  plastic scintillator bars, each layer perpendicular to the previous. With NeuLAND, the ToF, the deposited energy and hit position of the neutrons are measured. In front of NeuLAND, a VETO-wall is mounted to ignore measurements of charged particles from scattering that hit the detector. What is called NeuLAND in this setup is actually only a demonstrator detector for the full NeuLAND detector, which is being built for the new R<sup>3</sup>B setup at FAIR.

In addition to NeuLAND, also NEBULA [42] was used. It consists of two times two layers of  $120 \times 120 \times 1800 \text{ mm}^3$  plastic scintillators. All bars are oriented vertically and it is divided into two separate walls with two planes in each. There are also two VETO-walls installed, one in front of each NEBULA-wall to veto charged particles. NEBULA gives similar information as NeuLAND and the data from both detectors are combined to calculate the neutron multiplicity and ToF from the target.



## Chapter 3

# Detector Calibrations

In the SAMURAI-setup there are many different detectors (see Sec. 2.5.4). Each detector has several channels, up to 1600 for NeuLAND. Each of these channels have to be calibrated in order to obtain the measured time in absolute units of, e.g. ns, or the energy in units of MeV instead of channel numbers as is the case for the raw-data. How this is done depends on the detector type and in the following chapter I will describe the procedures I used for the different detectors in the SAMURAI setup. A significant part of the work in this thesis consisted in the calibration of all SAMURAI detectors. The coordinate system used in the description of the calibration and analysis is as follows. The  $z$ -axis runs in the same direction as the beam, the  $y$ -axis points upward, and to obtain a right handed coordinate system, the positive  $x$ -axis points to the left when looking in the beam direction.

### 3.1 Drift Chambers

In the setup there are four different drift chambers, two for tracking of the incoming ions and two for tracking the outgoing fragments, see Sec. 2.5.4. The measured quantity in these detectors are the drift times, i.e. the time it takes the electrons knocked out by the passing ion to drift to the closest anode wire. The drift time depends on the drift velocity of the electrons and the distance from the anode wire the ion passed. Since the drift velocity in the drift chambers to first approximation is constant, the drift time is directly proportional to the distance between the ion and the wire. In Fig. 3.1 the TDC-spectrum for one of the planes in FDC1 is shown. The conversion from TDC-channel to drift length is given by the formula

$$d_i = d_{\max} \frac{\sum_{j=i}^{b_{\max}} n_j}{\sum_{j=b_{\min}}^{b_{\max}} n_j} \quad (3.1)$$

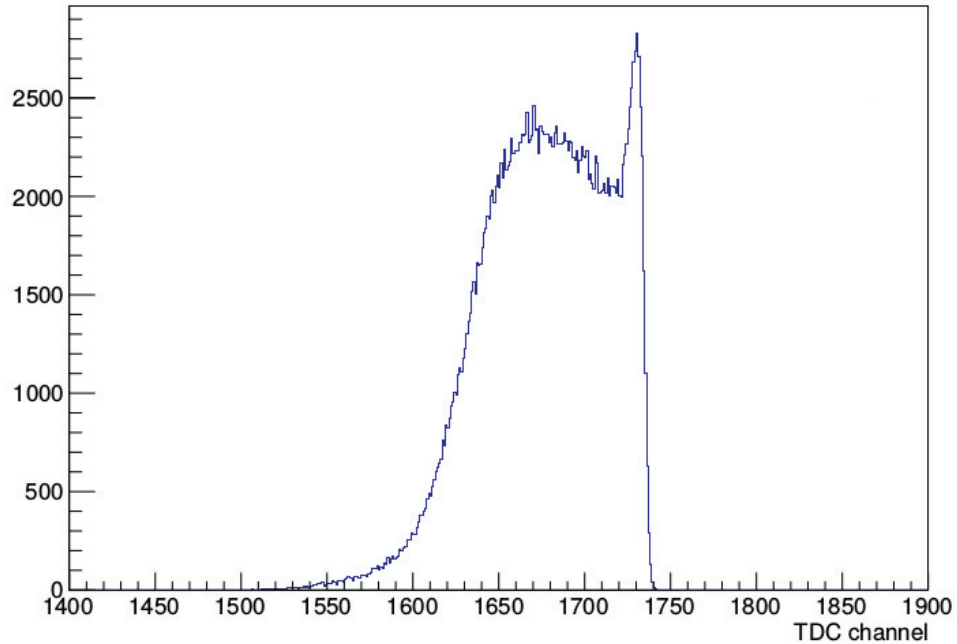


**Figure 3.1:** The TDC-spectrum from layer 1 in FDC1.

where  $d_i$  is the drift length for bin  $i$  in the TDC-spectrum,  $d_{\max}$  is the maximum drift length possible,  $b_{\min}$  and  $b_{\max}$  are the first and last bin with entries in the spectrum, respectively, and  $n_j$  is the number of entries in bin  $j$ . By doing this for all bins in the TDC spectrum a table is made, converting TDC-channels to drift lengths. As can be seen in Fig. 3.1 the spectrum is not uniformly distributed indicating that the drift velocity varies with the distance to the anode. Especially very close to the anode the drift velocity is high, which is why there is a peak at the right end of the spectrum.

While it is possible to obtain the distance from the anode to the ion passed from the drift time, the main problem is to tell if it passed on the right or left side of the anode wire. To solve this problem, data from the individual planes have to be combined. In the BDCs there are four  $x$ -planes and four  $y$ -planes. By taking the hits for one direction it should be possible to get a good linear fit for the hit positions since the ion should follow a straight trajectory through the detector. To decide if the drift length is positive or negative in a plane, the residual for each fit has to be considered. One simply fits all possible combinations of positive and negative drift lengths and checks which combination has the least total squared residual. When the best fit has been found, the residual for each plane can be plotted versus the tracked position as in Fig. 3.2. Here layer two in FDC1 is shown, it exhibits a clear dependence between the residual and the hit position. The periodicity in the dependence is the same as twice the maximum drift length

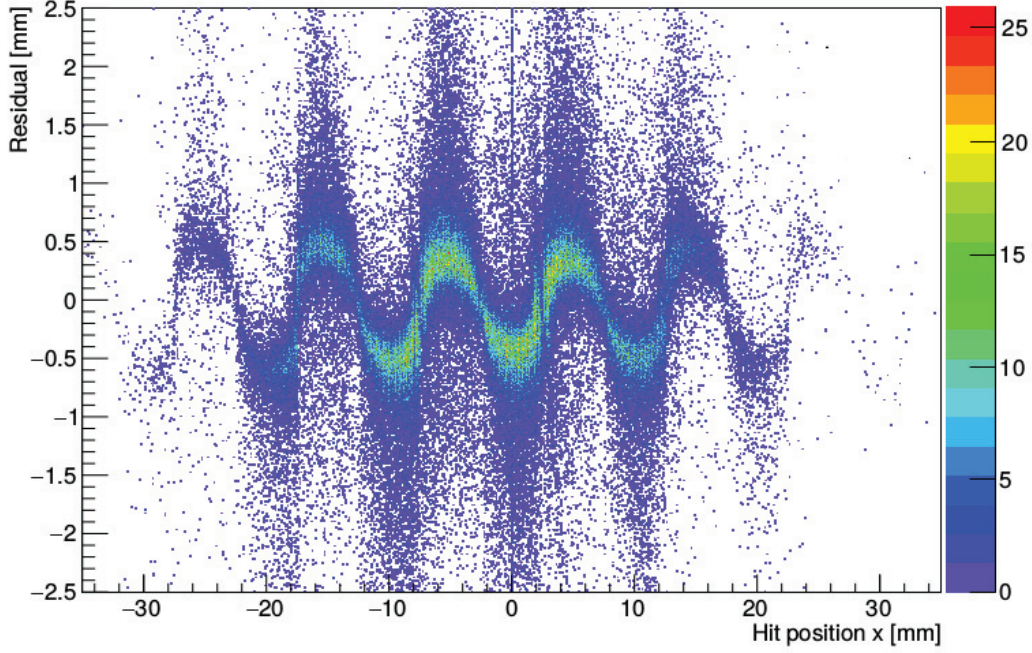


**Figure 3.2:** Residual plotted versus the tracked hit position in layer 2 in FDC1.

in FDC1 indicating the relation to the drift length.

To improve the drift length calibration this dependence has to be accounted for. This is done by fitting a 7<sup>th</sup> degree polynomial to each period which is then used to correct the drift length. Since this correction affects both the hit position and the fit, this has to be done several times in an iterative fashion. After four iterations the result has improved and is shown in Fig. 3.3.

For the BDCs the track is given by the  $x$ - and  $y$ -components, but for the FDCs there is no  $y$ -plane but instead a  $u$ - and a  $v$ -plane which are rotated  $30^\circ$  from the  $y$ -axis. To obtain the  $x$ - and  $y$ -components, these layers have to be combined also with the  $x$ -layers. This is done by a least square fit from the individual tracks already found in  $x$ -,  $u$ - and  $v$ -direction. The tracks in the  $x$ - and  $y$ -directions searched for are defined as

$$x = a + bz_i,$$

$$y = c + dz_i,$$

where  $a$ ,  $b$ ,  $c$  and  $d$  are the linear equation parameters and  $z_i$  is the position of each plane along the beam axis. We can also write the  $u$ - and  $v$ -positions in terms of  $x$  and  $y$  as

$$u, v = x \cdot \cos \theta_i + y \cdot \sin \theta_i$$

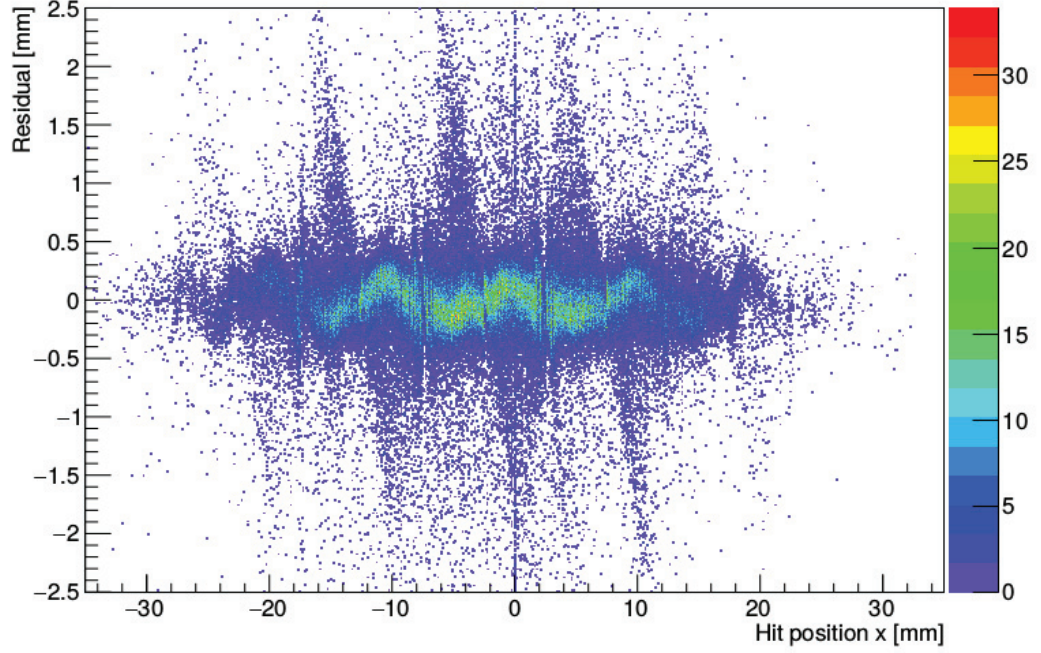


**Figure 3.3:** Residual plotted versus the tracked hit position in layer 2 in FDC1 after four iterations of calibration.

where  $\theta_i$  is the angle of the rotation, for  $u$  and  $v \pm 30^\circ$ . To find the values of  $a$ ,  $b$ ,  $c$  and  $d$  sum of the squares of the residuals in each plane has to be minimised. If the residual is denoted  $R$ , this can be written as

$$R^2 = \sum_{i=1}^{14} (x_i - ((a + bz_i) \cos \theta_i + (c + dz_i) \sin \theta_i))^2, \quad (3.2)$$

where  $x_i$  is the hit position in the internal coordinate system of layer  $i$ , i.e. it is either  $x$ ,  $u$ , or  $v$ , and the sum goes over all 14 planes in the FDCs. To minimise this function the derivative of each parameter in this equation has to be 0. The equation achieved can then be written as a matrix:

$$\begin{bmatrix} \sum \cos^2(\theta_i) & \sum z_i \cos^2(\theta_i) & \sum \cos(\theta_i) \sin(\theta_i) & \sum z_i \cos(\theta_i) \sin(\theta_i) \\ \sum z_i \cos^2(\theta_i) & \sum z_i^2 \cos^2(\theta_i) & \sum z_i \cos(\theta_i) \sin(\theta_i) & \sum z_i^2 \cos(\theta_i) \sin(\theta_i) \\ \sum \sin(\theta_i) \cos(\theta_i) & \sum z_i \sin(\theta_i) \cos(\theta_i) & \sum \sin^2(\theta_i) & \sum z_i \sin^2(\theta_i) \\ \sum z_i \sin(\theta_i) \cos(\theta_i) & \sum z_i^2 \sin(\theta_i) \cos(\theta_i) & \sum z_i \sin^2(\theta_i) & \sum z_i^2 \sin^2(\theta_i) \end{bmatrix} \begin{bmatrix} a \\ b \\ c \\ d \end{bmatrix} = \begin{bmatrix} \sum x_i \cos(\theta_i) \\ \sum x_i z_i \cos(\theta_i) \\ \sum x_i \sin(\theta_i) \\ \sum x_i z_i \sin(\theta_i) \end{bmatrix}$$

Note that the left matrix is constant for each layer and that it is only the right part which changes for each event. The solution to the equation system gives the linear components for the track in the  $x$  and  $y$  directions.

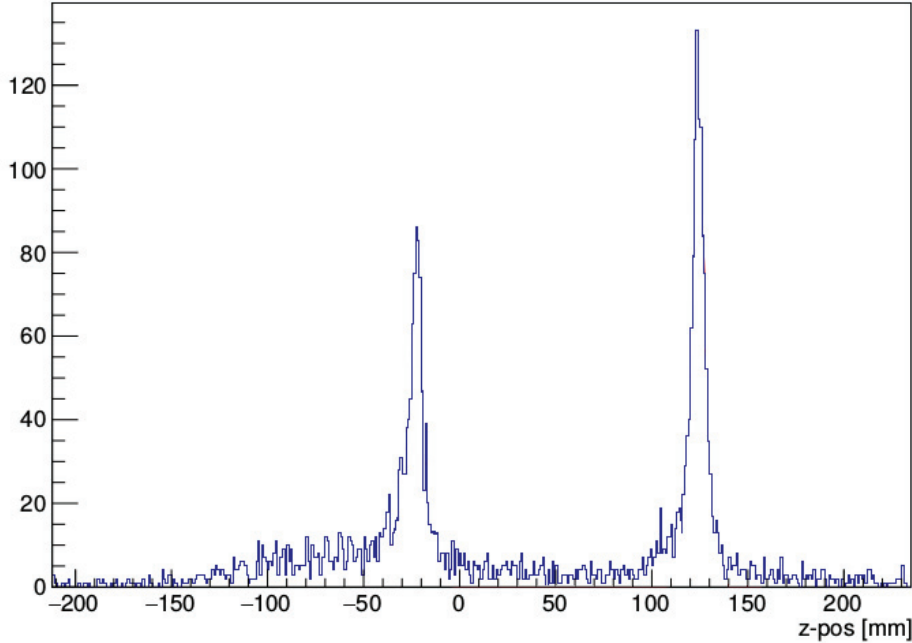


**Figure 3.4:** The reconstructed  $z$ -position in the MINOS TPC for an empty-target run, using two or more proton tracks. The two peaks occur due to the much enhanced reaction probability in the entrance and exit windows of the MINOS chamber.

## 3.2 MINOS TPC

The target MINOS, which is described in Sec. 2.5.4, consists both of a liquid hydrogen target and a TPC. To track the protons, the drift velocity in the TPC has to be calibrated. To do this an empty-target run is used. When the target chamber is empty, reactions can occur only in the entrance and exit windows of the target chamber. This can be seen in Fig. 3.4 where the reconstructed  $z$ -position is plotted. The two peaks are caused by the entrance and exit windows. The drift velocity can be calculated by the distance between the two peaks which corresponds to the distance between the entrance and exit windows.

When the drift velocity has been calculated, the position of the TPC relative to the drift chambers has to be considered. Especially the rotation around the beam axis has to be adjusted. This is achieved by a comparison of the hit positions at the target, extrapolated from the BDC drift chambers versus the vertex position given by the TPC. This comparison is shown in Fig. 3.5. There is an offset of about  $35^\circ$  between the angle given by the drift chambers and the one from the TPC, which is corrected.



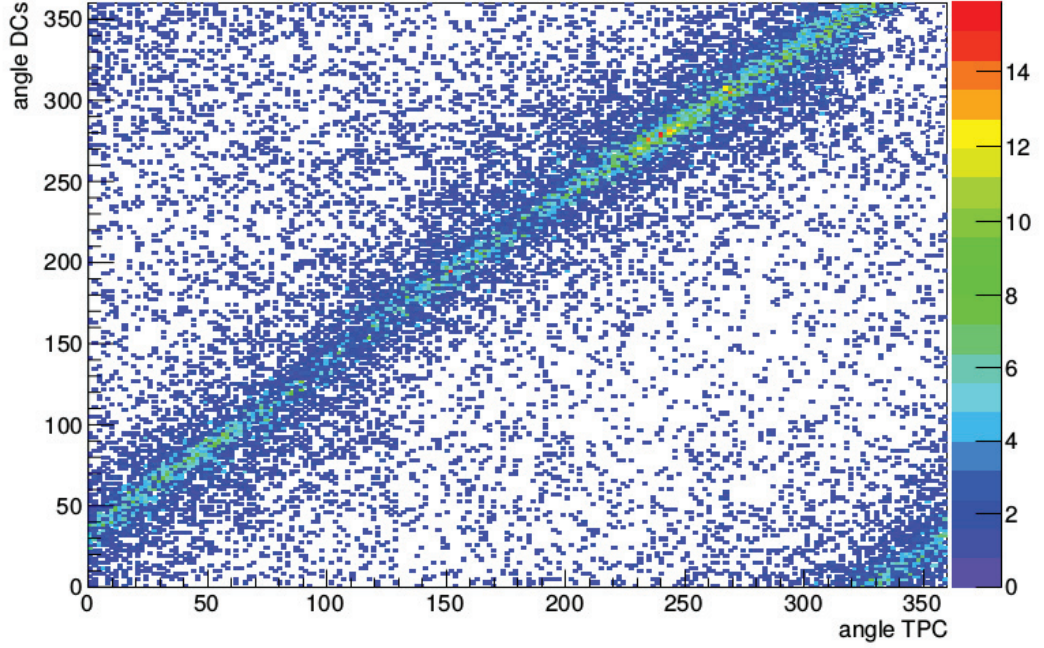


**Figure 3.5:** The angle calculated from the drift chambers plotted versus the angle given by the vertex position from the TPC. The offset is about  $35^\circ$ .

### 3.3 DALI2

The  $\gamma$ -detector DALI2 has both energy and time channels, which both need to be calibrated for each of the 142 crystals. This is done with three different sources,  $^{60}\text{Co}$ ,  $^{88}\text{Y}$  and  $^{137}\text{Cs}$ . Together, these sources give five visible  $\gamma$ -peaks at 661.7 keV, 898.0 keV, 1173.2 keV, 1332.5 keV and 1836.1 keV. These peaks are used to create a linear relation between QDC-channel and energy deposited. An example QDC-spectrum is shown in Fig. 3.6 where the five peaks are seen in the interval of channel 300 to 800.

### 3.4 Hodoscope

The hodoscope consists of 24 vertical plastic scintillator bars with one PM-tube at each end. The light produced in the scintillator when an ion passes is detected by both PM-tubes. Since the light produced needs some time to propagate from the hit position to the PM-tubes, the timing of the signals are different. The light is also attenuated in the scintillator which affects the energy readout in a similar way. Assume that the scintillator bar has the length  $2L$ , and is hit at position  $x$  at time  $T$ , as in Fig. 3.7. Then the

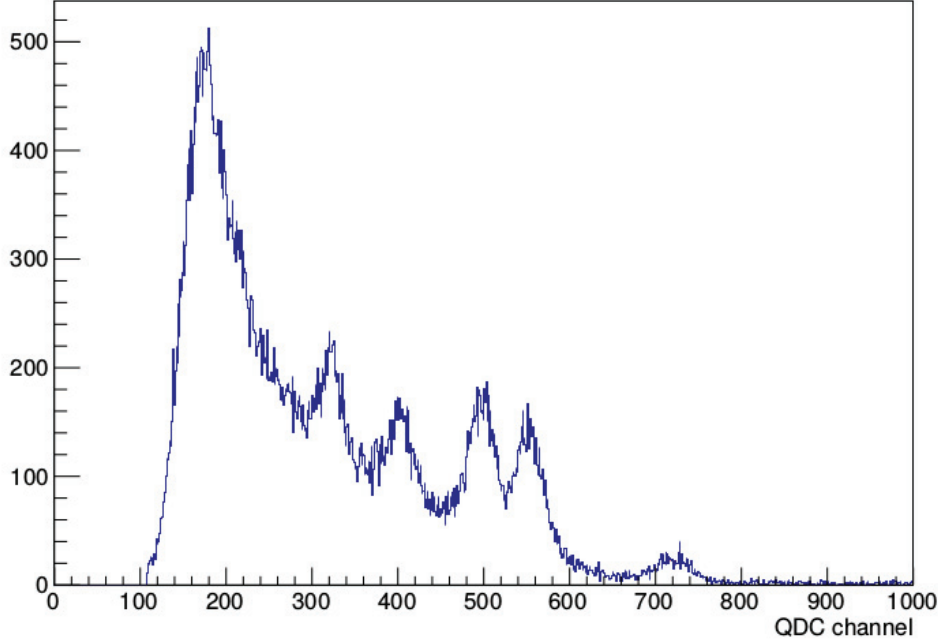


**Figure 3.6:** The QDC-spectrum for crystal number 80 in DALI2 using the sources  $^{60}\text{Co}$ ,  $^{88}\text{Y}$  and  $^{137}\text{Cs}$ . The five peaks in the channel range 300–800 correspond to transitions in the sources.

time signals given by the two PM-tubes are

$$\begin{aligned} t_1 &= T + \frac{L+x}{v}, \\ t_2 &= T + \frac{L-x}{v}, \end{aligned} \tag{3.3}$$

where  $v$  is the propagation speed of the light in the scintillator. To get the actual hit time  $T$ , the two equations are summed and divided by 2, giving

$$T = \frac{t_1 + t_2}{2} - \frac{L}{v}, \tag{3.4}$$

where the last term is a constant which can be included in the time offset calibration.

Taking the attenuation of the signals into account, the measured energy signals can be written as

$$\begin{aligned} e_1 &= E e^{-\frac{L+x}{\lambda}}, \\ e_2 &= E e^{-\frac{L-x}{\lambda}}, \end{aligned} \tag{3.5}$$

with  $E$  being the energy deposited in the scintillator and  $\lambda$  the attenuation length in the scintillator. Taking the square root of the product of  $e_1$  and  $e_2$  yields

$$E = e^{-\frac{L}{\lambda}} \sqrt{e_1 e_2}. \tag{3.6}$$

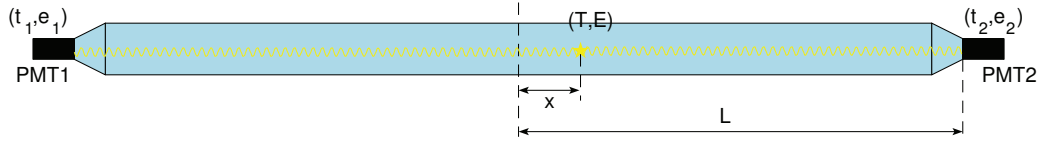


**Figure 3.7:** A scintillator bar with length  $2L$  is hit at position  $x$  with energy  $E$  deposited at time  $T$ . The two PM-tubes PMT1 and PMT2 give the time and energy signals  $(t_1, e_1)$  and  $(t_2, e_2)$ , respectively.

As was the case for the time signals, the term  $e^{\frac{L}{\lambda}}$  is a constant which can be included in the calibration parameters.

Both the time and the energy signals can also be used to calculate the hit position,  $x$ , in the scintillator. Using Eq. (3.3) and Eq. (3.5) the position can be written as

$$\begin{aligned} x &= \frac{v}{2}(t_1 - t_2), \\ x &= \frac{\lambda}{2} \ln \frac{e_2}{e_1}, \end{aligned} \tag{3.7}$$

where  $\frac{v}{2}$  and  $\frac{\lambda}{2}$  are constant scaling factors.

To calibrate the hodoscope it has to be ensured that the two PM-tubes are synchronised, i.e. that they give the same result for a hit in the centre of the paddle ( $x = 0$ ). Furthermore, each paddle has to be synchronised with all the other paddles in the detector so that the result does not depend on which paddle was hit. The first step of the calibration is to set the gain of the time and the offset for the energy. For this, a special so called Tcal-run is used. In this run no physics data is collected, instead start and stop signals are generated and sent to the TDCs. The time differences between the signals are a multiple of 10 ns, i.e. it can be 10, 20, 30... ns up to the range of the TDCs of about 300 ns. When looking at the time spectrum from the TDCs this generates a spectrum with sharp peaks, 10 ns apart. The gain is extracted by a linear fit of the peak positions in relation to the expected time difference. The energy offset is also taken from the Tcal-run. During this run no signals are present in the QDCs, so the measured energy should be 0. However, due to dark currents in the modules this is not the case. By plotting the energy spectrum the Gaussian peaks appear slightly above 0. The energy offset is found using Gaussian fits of these peaks.

The time offset has to be set in three steps. First the time offset between the two PM-tubes in the same bar is synchronised. This is done using a sweep-run. In this run a  $^{20}\text{F}$  beam was used, impinging on a thick copper target. During the run the magnetic field of SAMURAI was gradually changed such that the beam hit different parts of the hodoscope. By using FDC2, the hit position at the hodoscope can be extrapolated. The time difference between the PM-tubes as a function of the hit position in the  $y$ -direction are considered. For hits in the centre of each paddle, the time



difference should be 0.

When all bars are internally time calibrated the bars are synchronised with respect to each other. This is also done using the sweep run. Since the magnetic field is changing, so is the path of the ions through the magnet, and thus also the ToF is different even if the beam velocity is the same. Therefore, two bars should not measure the same ToF if the velocity is identical. However, events which have hits at the adjacent edges of two neighbour bars should give, within the resolution of the time measurements, the same ToF. The hit position at the hodoscope is extrapolated from FDC2. Starting from one side of the hodoscope the adjacent bar is synchronised so that hits within 1 cm from the edge matches the ToF within one 1 cm of the other bar. This is done step by step for all the bars and in the end the detector is internally calibrated.

What is left is to set the time offset for the entire detector relative the rest of the setup. This is probably the trickiest part of the calibration because the ToF has to be known, but it is the detector measuring the ToF which has to be calibrated. Hence, it is hard to use any data and instead simulations are used. The entire setup is simulated starting from the SBT and all detectors and magnetic fields are included up to the hodoscope. From the simulations the expected ToF is obtained which then can be used to set the time offset. The final time signals for each bar can then be written

$$\begin{aligned} t_1 &= t_{1,\text{raw}} \cdot g_1 + t_{\text{diff}} + t_{\text{det}} + t_{\text{setup}}, \\ t_2 &= t_{2,\text{raw}} \cdot g_2 - t_{\text{diff}} + t_{\text{det}} + t_{\text{setup}}, \end{aligned} \tag{3.8}$$

where  $g_{1,2}$  are the gain factors,  $t_{\text{diff}}$  the time offset between the two PM-tubes,  $t_{\text{det}}$  the time offset between the different bars and  $t_{\text{setup}}$  the time offset towards the rest of the setup.

The energy calibration is also done using the data from the sweep run. Since the magnetic field in SAMURAI is changing, nuclei of the same isotope and with the same energy hit all the bars in hodoscope. The energy loss in a plastic scintillator for a given isotope and velocity can easily be calculated using the Bethe-Bloch formula or from simulations. By identifying the ions hitting the hodoscope and measuring their velocity it is possible to set a gain factor to match the expected energy loss given by simulations. One thing which has to be taken into account, though, is the position dependence as shown in Eq. (3.5). If the statistics is high, the calibration can be done using events only hitting in the centre of the detector, otherwise the measured energy in each PMT has to be corrected for the hit position.

### 3.5 NeuLAND and NEBULA

The calibration of NeuLAND and NEBULA is very similar to that of the hodoscope. The difference is that instead of using a sweep-run to calcu-

late the time offsets, cosmic muons are used. Cosmic muons are minimum ionising particles passing through the entire detectors close to the speed of light. In NeuLAND it is possible to track the trajectory of the muons using all the bars in the detector. In NEBULA all bars are mounted vertically and hence it is not possible to track the muons in the same way as in NeuLAND. Instead 16 extra horizontal bars are mounted in front of, in between and behind the NEBULA planes. If two or more of these bars are hit it is possible to reconstruct the trajectory of the muon and hence also use it for calibration. The reason it is important to track the muons is the same as for the hodoscope, the signals depend on the hit position in the bar.

While muons are used to calibrate the detector internally, calibrating the time offset to the rest of the setup requires experimental data to be used. Using the same beam and target as for the sweep run, many events have  $\gamma$ -rays created at the target. These travel at the speed of light and can be detected by the neutron detectors. Since the flight distance of the  $\gamma$ -rays can be calculated from the detector and target position, it is straight forward to also calculate the expected ToF for the  $\gamma$ 's and set the time offset accordingly. All this leads to the same equation for the times as in Eq. (3.8) for each bar in both NeuLAND and NEBULA.

## Chapter 4

# Unbound states in $^{29}\text{Ne}$

The structure of light neutron-rich nuclei has been studied frequently and much of the attention has been drawn to the so-called island of inversion. The reason is that in this region of the chart of the nuclides the traditional shell closures at  $N=20$  and  $N=28$  breaks down. This is believed to be caused by intruder states from the  $fp$ -shell [10, 11]. This also gives rise to possible shape coexistence [12, 13]. As the  $1d_{3/2}$  and  $1f_{7/2}$  states move closer together the shell gap at  $N=20$  breaks down [43]. It also means that contributions from  $f_{7/2}$  configurations are expected at low excitation energies or even as significant part of the ground state wave function for nuclei in this region. The nucleus  $^{29}\text{Ne}$  lies on the border of the island of inversion and is thus expected to have low-lying  $f$ -wave strength. In the latest report on excited states in  $^{29}\text{Ne}$  by Liu *et al.* [44], no states were found which could be assigned to a  $7/2^-$  state. As the binding energy in  $^{29}\text{Ne}$  is low, 0.96 MeV [45], it is possible that the  $f_{7/2}$  strength is unbound.

As reported in Refs. [8, 46],  $^{29}\text{Ne}$  may exhibit a moderate  $p$ -wave halo structure or at least an extended spatial distribution. Moreover, Ref. [46] concludes that  $^{29}\text{Ne}$  is deformed, based on 1-neutron removal reaction cross sections. The ground state of  $^{29}\text{Ne}$  has  $J^+ = 3/2^-$  [46] with a low-lying  $3/2^+$  state, while so far, no low-lying  $7/2^-$  state has been found. This places  $^{29}\text{Ne}$  firmly into the island of inversion [44], and makes it, possibly, one of the heaviest halo nuclei found to date. Nevertheless, the missing  $f$ -wave strength at low excitation energies remains a puzzle that warrants further investigation.

The two previous studies of  $^{29}\text{Ne}$  by Belleguic *et al.* [47] reported an excited state at 680(60) keV and Liu *et al.* [44] reported three excited states at 222(4) keV, 620(4) keV and 923(10) keV. These are the only excited states in  $^{29}\text{Ne}$  which have been found to date. In this chapter I present the results of the first measurements of unbound states in  $^{29}\text{Ne}$ .

## 4.1 Experiment

The experiment was performed at the RIKEN Nishina Center for Accelerator-Based Science in November to December 2015 using the SAMURAI setup described in Sec. 2.5.3 and 2.5.4. The radioactive beam was created from a primary beam of  $^{48}\text{Ca}$  with an energy of 345 MeV/nucleon impinging on a beryllium target. With BigRIPS a cocktail beam consisting mostly of  $^{29}\text{F}$  and  $^{30}\text{Ne}$  was created from the reaction fragments and transmitted to the SAMURAI setup<sup>1</sup>. When reaching the experimental setup, the energy of the beam was in the interval 255 – 270 MeV/nucleon. The target consisted of the 15 cm long liquid hydrogen target MINOS, described in Sec. 2.5.4.

The main goal of the experiment was to study the unbound and doubly magic nucleus  $^{28}\text{O}$ , but also the unbound nuclei  $^{27}\text{O}$  and  $^{28}\text{F}$ , via one and two proton knock-out reactions from  $^{29}\text{F}$  and  $^{29}\text{Ne}$ . The focus of this work, however, is on unbound states in  $^{29}\text{Ne}$  studied via one neutron knock-out reactions from  $^{30}\text{Ne}$ . The calibration of the detectors in the setup is described in Ch. 3, hence in this chapter only the analysis and results are discussed.

## 4.2 Data Analysis

The incoming ions are identified via the ToF from the fragment separator to the SBT detectors, the energy loss in the SBT detectors and the  $B\rho$  setting of the fragment separator. As the energy loss, according to the Bethe-Bloch formula, is proportional to  $Z^2$ , the charges of the ions are given by the energy loss measurement. The magnetic rigidity can be calculated event-by-event using the offset from the centerline,  $x_{f5}$ , at the focal plane in-between the two separator steps in BigRIPS,

$$B\rho = \left(1 + \frac{x_{f5}}{d}\right)B\rho_0, \quad (4.1)$$

where  $d$  is the momentum dispersion, which is a measured quantity of the separator, and  $B\rho_0$  is the nominal magnetic rigidity set in the separator. Using this equation to calculate the magnetic rigidity in combination with Eq. (2.7), the mass-over-charge ratio can be calculated as

$$\frac{A}{Z} = \frac{e \cdot B\rho}{m_u \gamma \beta c}, \quad (4.2)$$

where  $m_u$  is the atomic mass unit.

The outgoing ions are identified in a similar way. The charge is extracted from the energy loss in the hodoscope, while the-mass-over charge ratio is given by the ToF from the vertex position to the hodoscope, in combination

---

<sup>1</sup>Also another setting in BigRIPS was used to create a beam consisting mostly of  $^{29}\text{Ne}$  and  $^{30}\text{Na}$ , which is not part of this work.

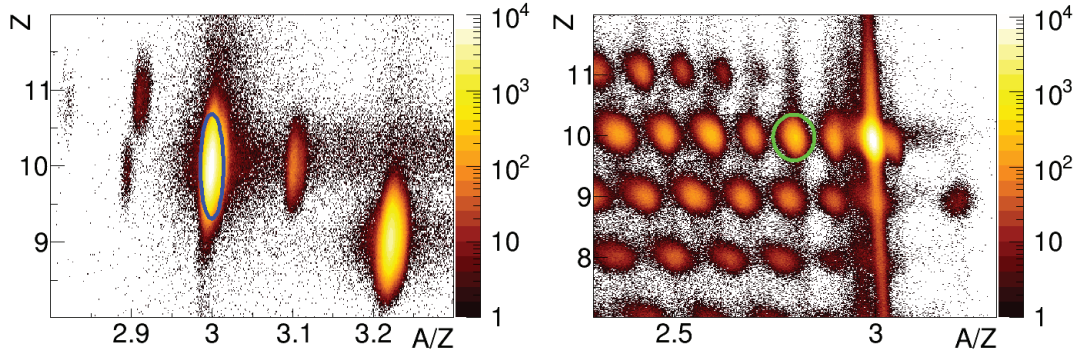


**Figure 4.1:** Identification plots of the incoming (left) and outgoing (right) ions. The blue and green ellipses show the acceptance condition for the incoming  $^{30}\text{Ne}$  and outgoing  $^{28}\text{Ne}$  ions, respectively. The outgoing identification plot only includes events where the incoming ion was identified as  $^{30}\text{Ne}$ .

with the trajectory of the ion measured with the drift chambers FDC1 and FDC2. Since the ToF is measured between the SBT and the hodoscope, the ToF to the vertex position has to be subtracted from the measured value. This is done based on simulations in Geant4 [48], taking the energy losses in all detectors in-between into account. Once the identifications of the incoming and outgoing ions are done, a selection of a reaction channel can be made. In Fig. 4.1, the identification of the incoming and outgoing ions is presented together with the conditions used to select the reaction channel. To study unbound states in  $^{29}\text{Ne}$  from one-neutron knock-out reactions in  $^{30}\text{Ne}$ , a selection of incoming  $^{30}\text{Ne}$  and outgoing  $^{28}\text{Ne}$  is used. In addition, two more conditions have to be fulfilled. First, one neutron has to be detected in the neutron detectors, and second, there has to be one proton track in MINOS. The first condition is necessary as the neutron is part of the unbound  $^{29}\text{Ne}$  consisting of  $^{28}\text{Ne} + n$ . A detailed description about how the neutron multiplicity is calculated is given later. The second condition ensures that the neutron knockout reaction took place in the hydrogen target and that the vertex position can be determined.

The vertex position is calculated using a combination of the proton track given by the MINOS TPC and the incoming ion track given by the two BDC drift chambers. The vertex position is given by the intersection point of these two tracks. However, due to uncertainties in the track measurements, the tracks do not exactly coincide. Instead the vertex position is taken as the middle point on the shortest possible line connecting the two trajectories. To avoid events with a large uncertainty in the vertex position, a condition is applied where only events with a the minimum distance less than 2 mm are accepted.

The detection of neutrons in the setup is essential to perform a complete-

kinematics experiment. The problem of neutron detection is that neutrons are non-ionising, thus they cannot be seen directly in a scintillator. By nuclear reactions, however, charged particles are released, which in turn can be detected by the scintillator. But only detecting secondary particles is also problematic, mainly because the neutrons almost always deposit only a part of their kinetic energy and it is hard to track them through the detector. As a consequence, if two hits are recorded in the detector it is difficult to tell if they were caused by one neutron interacting two times in the detector or if two neutrons interacted in the detector. This, of course, becomes more and more complicated the more neutrons that hit the detector each event.

In this setup, in principle three neutron detectors have been used, NEULAND and NEBULA which is subdivided into two walls. A detailed description of these detectors is given in Sec. 2.5.4. The analysis of the data from the detectors is done in two steps. In the first step each wall is handled individually. For each wall, all hits are collected and sorted according to the time of the hit. Then the first hit is compared with all other hits in the wall. If the spatial distance between the hits is less than 20 cm and the time difference between the hits is less than 2 ns, they are considered to originate from the same neutron and are clustered together. This comparison is made between all hits until all clusters have been identified<sup>2</sup>. There is one additional condition on the clusters, namely that the total deposited energy in each cluster should be larger than 5 MeV, otherwise it is discarded [49].

The second step to calculate the neutron multiplicity is to combine the clusters in the three different walls. If a neutron interacts in the first wall, it loses kinetic energy. That means that its velocity decreases. Thus, if a neutron interacts both in the first and in the second wall, the velocity between the target and the first hit, denoted  $\beta_{01}$ , has to be larger than the velocity between the first and second hit in the detectors, denoted  $\beta_{12}$ . The two clusters are considered originating from the same neutron if  $\beta_{01} > \beta_{12}$ . When this is the case, the cluster in the second wall is dismissed. Once the velocity comparisons have been made between all clusters, the total neutron multiplicity is the number of clusters left. This is a rather simple method of combining clusters and if there are several clusters in each wall one also has to take into account which clusters to combine as that may affect the neutron multiplicity. In this work, though, this is not important as only events with one neutron are used. Hence, if there are several hits in each wall these events are discarded, as that means that there has to be more than one neutron hitting the detectors.

---

<sup>2</sup>A cluster can consist of only one hit, if no other hits fulfil the requirement of space and time proximity.



**Table 4.1:** The expected number of  $\gamma$ -rays emitted from the sources.

Source	Activity [kBq]	Energy [keV]	Branching ratio [%]	Measurement time [s]	DAQ live time [%]	Down-scale factor	Number $\gamma$ s $10^6$
$^{137}\text{Cs}$	7.22	662	94.7	900	24.6	1	1.51
$^{60}\text{Co}$	41.6	1173	99.9	1200	50.6	10	2.53
$^{60}\text{Co}$	41.6	1332	100	1200	50.6	10	2.53
$^{88}\text{Y}$	2.46	898	93.7	1800	28.6	1	1.19
$^{88}\text{Y}$	2.46	1836	99.2	1800	28.6	1	1.26

### 4.3 Detector Efficiency and Acceptance

The detection efficiency of the fragments is close to 100% in the drift chambers and the hodoscope. This is not the case for the uncharged  $\gamma$ -rays and neutrons. The detection efficiency in the neutron detectors NeuLAND and NEBULA depends on the kinetic energy of the neutrons. The mean free path of a neutron in NeuLAND is about 100 cm for 250 MeV neutrons [50], which is the energy of the neutrons detected in the experiment. This means that the probability of detecting one neutron in NeuLAND is around 33%. What further limits the neutron detection is the acceptance of the detectors. This is given by the size of the detectors and the aperture of the SAMURAI magnet. The acceptance affects the relative energy measurements as it decreases with increasing relative energy. To take this effect into account, simulations were performed using GEANT4 [48] and the wrapper program GGLAND [51], to find the total detection efficiency of neutrons as a function of the relative energy.

In the simulations, the SAMURAI magnet was placed together with the neutron detectors, NeuLAND and NEBULA according to the experimental setup. A  $^{28}\text{Ne}$  ion was generated with velocity  $\beta = 0.6$  and an angular spread similar to the experimental data. In coincidence, a neutron was generated with a relative energy to the fragment ranging between 0 – 10 MeV. From the simulated response of the neutron detectors, the relative energy was reconstructed. Since the generated relative energy is known, the probability of reconstructing the correct value can be calculated as a function of the relative energy. The result of this calculation is shown in Fig. 4.2.

Also the  $\gamma$ -rays suffer from a limited detection efficiency and acceptance. To find the total detection efficiency as a function of the  $\gamma$ -energy, the source runs, which were used for energy calibration, are used. The sources have a known activity. From the activity it is possible to calculate the number of emitted  $\gamma$ -rays. By comparing this to the number of detected  $\gamma$ -rays, the detection efficiency for a given energy can be extracted. Tab. 4.1 summarises the different sources and expected number of  $\gamma$ -rays emitted and detectable.

The number of detected  $\gamma$ -rays are extracted from the experimental data using a Gaussian fit together with an exponential background. This is done for all the five photo-peaks in the spectra and the efficiency is plotted in

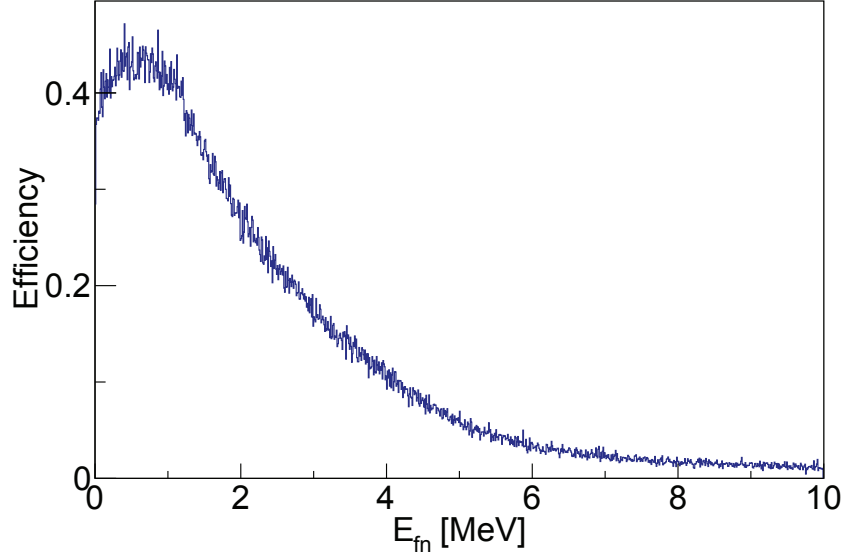


**Figure 4.2:** The neutron detection efficiency and acceptance as a function of the relative energy between the neutron and fragment. The efficiency at lower energies is decided by the detection efficiency, while the decrease at higher energies is due to acceptance.

Fig. 4.3 as a function of the  $\gamma$ -energy. To these data points an exponential function is fitted, which models the response function of the detector.

## 4.4 Results and Discussion

For events fulfilling all the aforementioned conditions, the 4-momentum vectors of the outgoing  $^{28}\text{Ne}$  and the neutron are calculated. These are used to extract the relative energy of the  $^{28}\text{Ne} + n$  system calculated according to Eq. (2.5). The relative energy is also corrected for the efficiency and acceptance of the neutron detection in accordance with Fig. 4.2. The result is presented in Fig. 4.4 together with fits of three Breit-Wigner peaks [52] on the form

$$f_l(E; E_r, \Gamma_l) = \frac{\Gamma_l(E)}{(E - E_r)^2 + \frac{\Gamma_l(E)^2}{4}}, \quad (4.3)$$

where  $E_r$  is the resonance energy,  $E$  the relative energy and  $\Gamma_l(E)$  is the apparent width. The apparent width depends on the relative energy and the angular momentum  $l$ . It is calculated as

$$\Gamma_l(E) = 2\Gamma_r^2 P_l(\rho, \eta), \quad (4.4)$$

where  $\Gamma_r$  is the resonance width and  $P_l(\rho, \eta)$  the penetrability factor with  $\eta$  being the Coulomb field parameter, which for neutrons is 0, and  $\rho$  depends



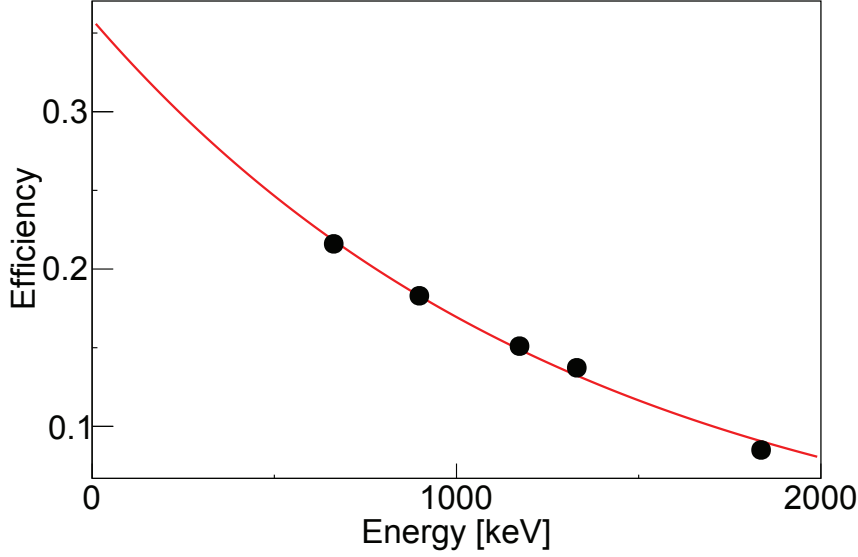


**Figure 4.3:** The  $\gamma$  detection efficiency as a function of energy. The red line is an exponential fit to the five data points. The function of the fit is used to calculate the efficiency for any given  $\gamma$ -energy.

on the reduced mass of the system ( $\mu$ ), the relative energy ( $E$ ), the channel radius ( $R$ ) and the reduced Planck constant ( $\hbar$ ), as

$$\rho = \frac{R\sqrt{2\mu E}}{\hbar}. \quad (4.5)$$

The value of  $R$  does not have a large impact on the final resonance energies, which has also been pointed out in e.g. Ref. [53]. In the following analysis,  $R = 5$  fm has been used. The penetrability factor for neutrons with  $l = 0, 1, 2, 3$  are as follows

$$\begin{aligned} P_0(\rho) &= \rho; \\ P_1(\rho) &= \frac{\rho^3}{1 + \rho^2}; \\ P_2(\rho) &= \frac{\rho^5}{9 + 3\rho^2 + \rho^4}; \\ P_3(\rho) &= \frac{\rho^7}{225 + 45\rho^2 + 6\rho^4 + \rho^6}. \end{aligned} \quad (4.6)$$

Fits were done using all possible combinations of angular momenta of the three peaks. The combination with the smallest reduced  $\chi^2$  was found with  $l = 0$  at 0.34 MeV (green),  $l = 2$  at 0.62 MeV (blue) and  $l = 2$  at 1.67 MeV (purple). The width of the peaks are 0.61, 3.09 and 1.82 MeV, respectively. For the fit in Fig. 4.4  $\chi^2 = 3.2$ . It should be noted though, that several different combinations of  $l$  gave similar  $\chi^2$  values of 3.2–4.0. Hence, it is

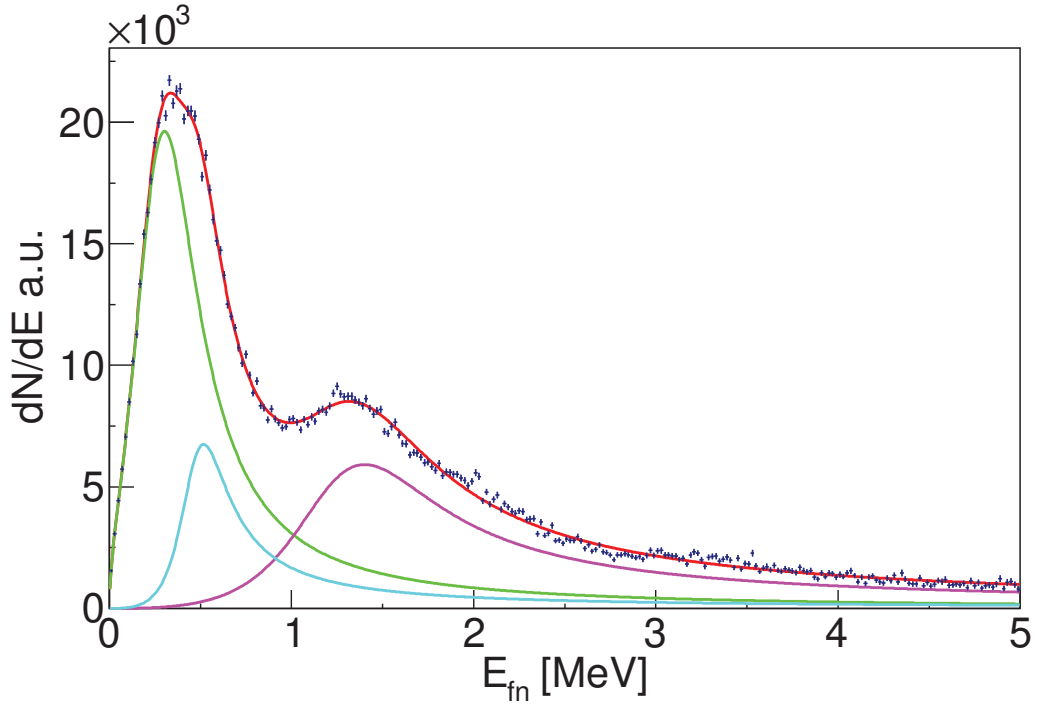


**Figure 4.4:** The relative energy spectrum for unbound  $^{29}\text{Ne}$  together with a fit consisting of a linear combination of three Breit-Wigner functions. The fit result of the Breit-Wigner functions are given in green, purple and blue, while the total fit is shown in red. The peak positions of the Breit-Wigner functions are 0.34 MeV (green), 0.62 MeV (blue) and 1.67 MeV (purple).

not possible to decide whether the values assigned in the fit are the correct values of the orbital angular momentum for the resonances.

When the unbound  $^{29}\text{Ne}$  decays, the daughter nucleus  $^{28}\text{Ne}$  may end up in an excited state. This state decays via  $\gamma$ -decay which can be detected with the  $\gamma$ -detector DALI2. Since the  $\gamma$ -photons may Compton scatter and deposit energy in several different crystals an add-back routine is used to add the energy of neighbouring crystals. In addition, the  $\gamma$ -energy is corrected for the Doppler effect. In Fig. 4.5 the resulting energy spectrum in coincidence with the detection of unbound  $^{29}\text{Ne}$  is presented. Four  $\gamma$ -peaks are found, at 910, 1130, 1325 and 1585 keV. These states have all been previously observed and are reported in Refs. [46, 47, 54].

The excitation energy  $E_{\text{exc}}$ , of the unbound  $^{29}\text{Ne}$  is calculated from the relative energy  $E_{\text{fn}}$ , neutron separation energy  $S_{\text{n}}$  and  $\gamma$  excitation energy  $E_{\gamma}$  as

$$E_{\text{exc}} = S_{\text{n}} + E_{\text{fn}} + E_{\gamma}. \quad (4.7)$$

The neutron separation energy of  $^{29}\text{Ne}$  is 0.96 MeV [45]. To get the excitation energy, the  $\gamma$ -energy spectrum has to be correlated with the relative energy. This correlation is shown in Fig. 4.6 and it can be concluded that

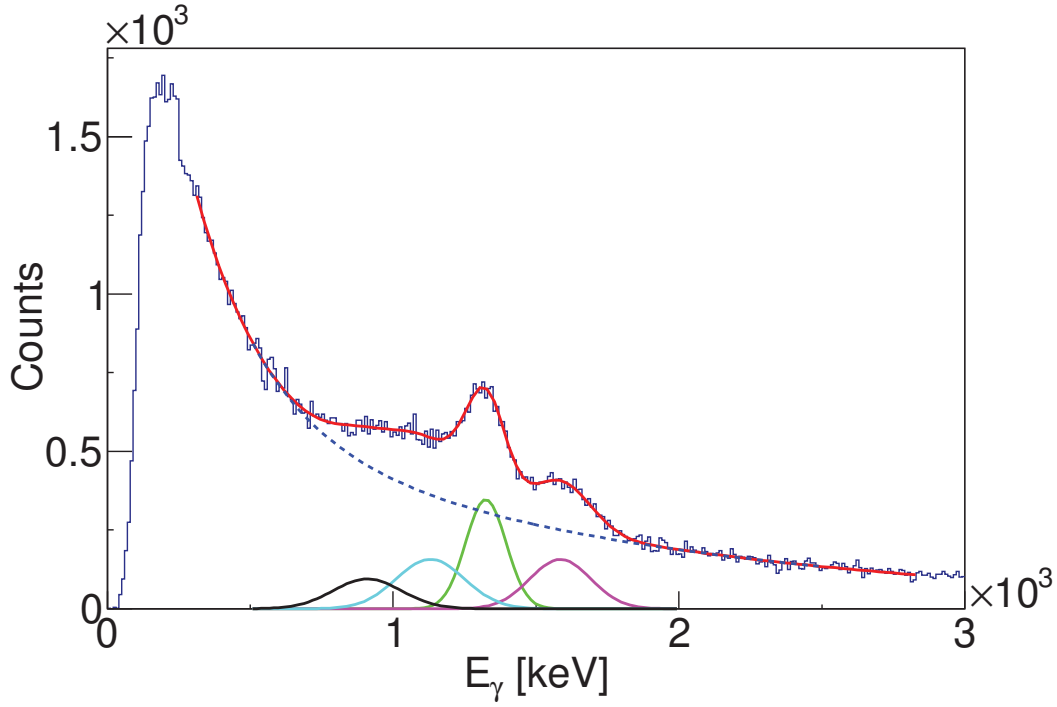


**Figure 4.5:** The Doppler-corrected  $\gamma$ -energy spectrum taken in coincidence with the unbound  $^{28}\text{Ne}+n$  system. The data is fitted with two exponential functions for the background, and four Gaussian peaks corresponding to four different excited states in  $^{28}\text{Ne}$ . Two are found at 1325 keV and 1585 keV, green and purple curves, while two more peaks are located at 910 keV and 1130 keV, black and blue curve. The background is indicated with the blue dashed line, while the total fit is shown by the red curve.

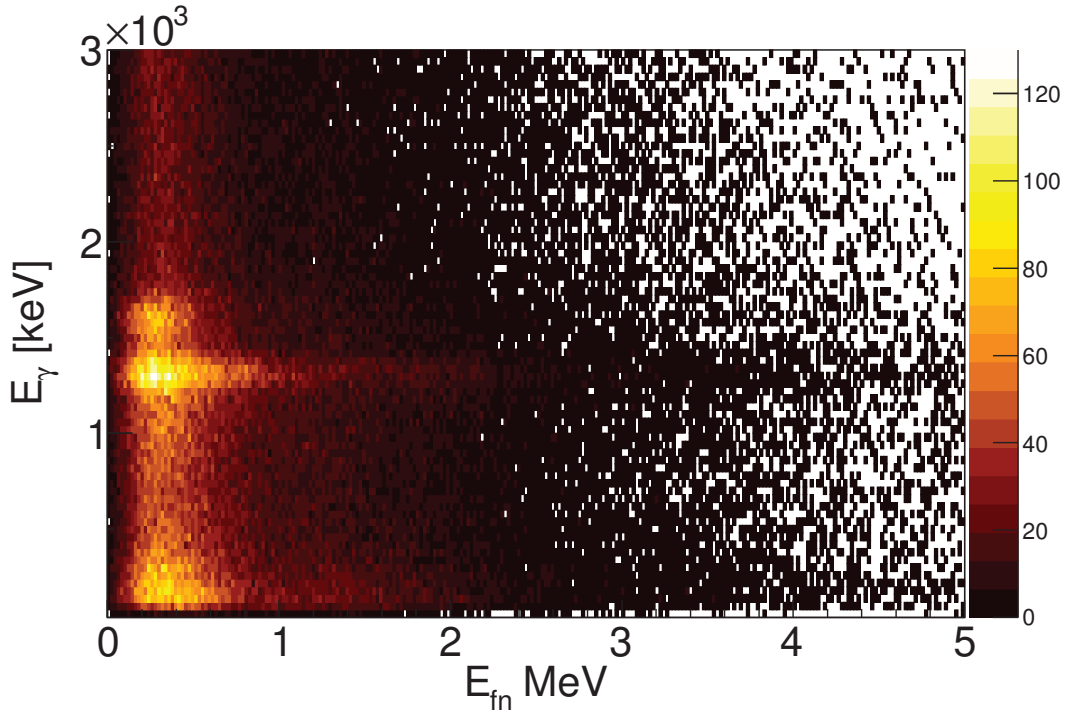


**Figure 4.6:** The  $\gamma$  energy in coincidence with the relative energy. Events with  $E_\gamma = 0$  are suppressed. The two peaks in the relative energy spectrum (Fig. 4.4) are in coincidence with the two clear  $\gamma$ -peaks in Fig. 4.5 meaning that this excited state in  $^{29}\text{Ne}$  feeds two different excited states in  $^{28}\text{Ne}$ .

the two photopeaks in Fig. 4.5 are in coincidence with the two lower energy peaks in the relative energy spectrum. It is hard to conclude which of the two peaks are in coincidence with the  $\gamma$ -rays from this spectrum. To investigate this it is useful to look at the relative energy spectrum for the two different cases when  $\gamma$ -rays have been detected with 1325 keV or with 1585 keV, which is shown in Fig. 4.7. This could also be done for the other two peaks in the  $\gamma$ -spectrum, but because they have a large background contribution and are also not well separated, they have not been considered in this analysis.

The shape of the Breit-Wigner peaks depend on the angular momentum of the nucleus, which in turn depends on which neutron was knocked out in the (p,pn) reaction. As mentioned earlier, when fitting the peaks in the relative energy spectrum, several different combinations of angular momenta give similar  $\chi^2$  values. To find out which combination is the most likely, it is useful to know which peak is expected to have the higher angular momentum. This can be found out by investigating the longitudinal momentum distribution of the outgoing fragment in the center-of-mass frame of the incoming ion. In Fig. 4.8, this distribution is shown for the outgoing  $^{28}\text{Ne}$  fragment.

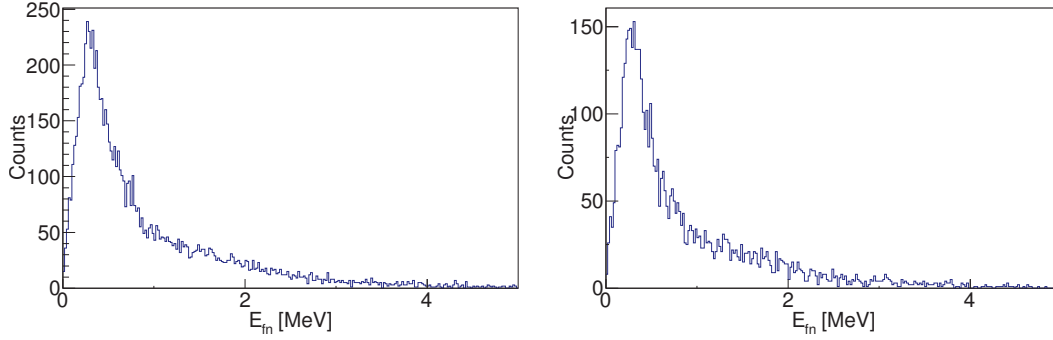


**Figure 4.7:** The relative energy spectra in coincidence with 1325 keV  $\gamma$ -rays, left, and 1585 keV  $\gamma$ -rays, right. No major difference can be noticed between them, indicating that they originate from the same state in  $^{29}\text{Ne}$ .

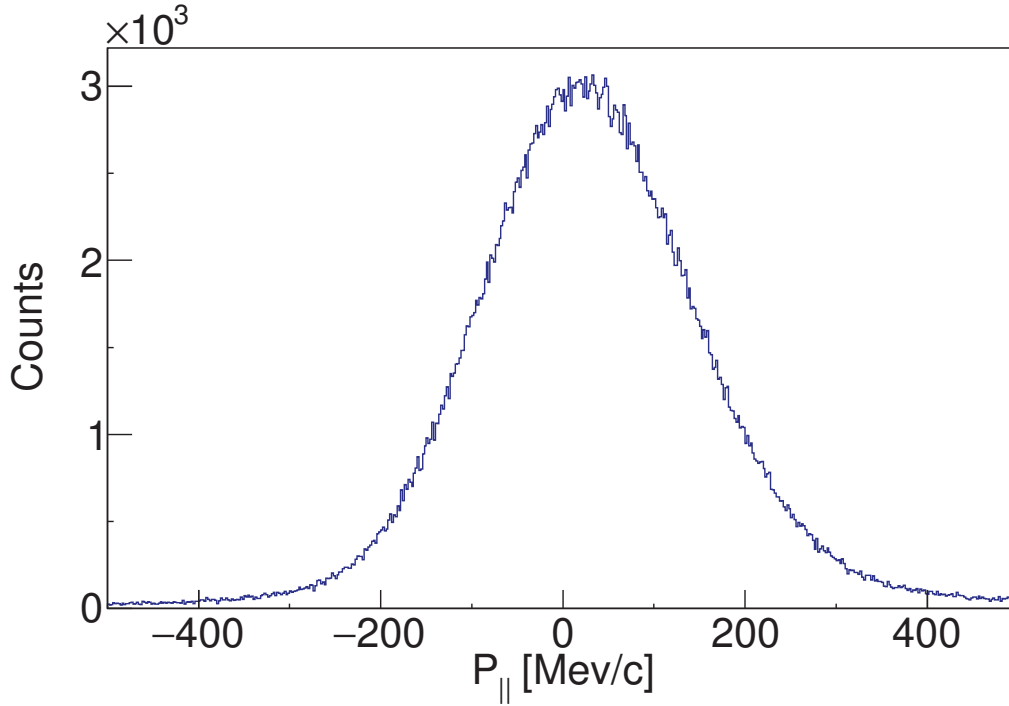


**Figure 4.8:** The longitudinal momentum distribution of  $^{28}\text{Ne}$  fragments in the center-of-mass frame of the incoming  $^{30}\text{Ne}$  ions.

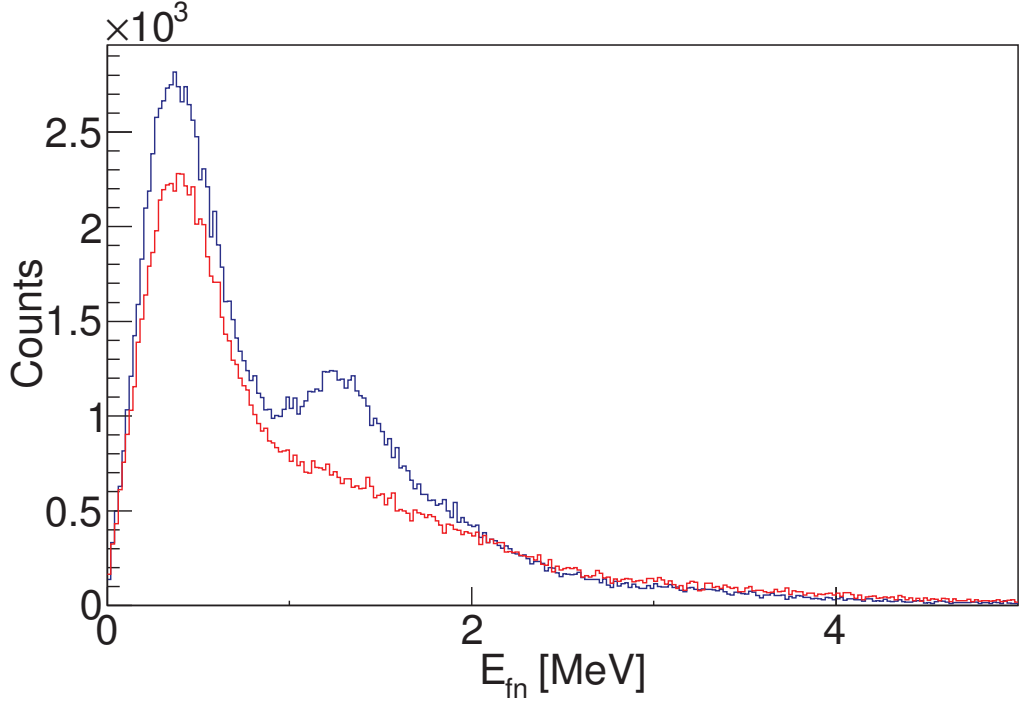


**Figure 4.9:** The relative energy for two different cases. Blue line when  $|P_{||}| < 50$  MeV/c and red line when  $|P_{||}| > 150$  MeV/c. The clear enhancement of the peak around 1.3 MeV for events with a large longitudinal momentum suggests that this peak should be fitted with a Breit-Wigner function with a low angular momentum.

If a neutron from a low  $l$ -orbital is knocked out, the spread in the longitudinal momentum is expected to be narrow. If a neutron from a higher  $l$ -orbital is knocked out, the spread in the longitudinal momentum is expected to be wider. This means that it is more likely that a neutron from a high  $l$ -orbital was knocked out in events with a large longitudinal momentum. In Fig. 4.9 the relative energy is shown for two cases. The blue line is when  $|P_{||}| < 50$  MeV/c and the red line when  $|P_{||}| > 150$  MeV/c. It is clear that the peak around 1.3 MeV is enhanced for events with small longitudinal momentum and it can be concluded that this should correspond to a lower orbital angular momentum state.

This check can also be done the other way around by looking at the longitudinal momentum distribution for the different peaks in the relative energy spectrum. In Fig. 4.10 the longitudinal momentum distribution is shown for the lower energy peak in the relative energy spectrum in blue, the higher lying energy peak in red, and the green curve is the same histogram as the red but scaled to the same number of events as the blue histogram for easier comparison. The blue histogram is slightly wider than the green which is in agreement with the previous conclusion that the lower energy

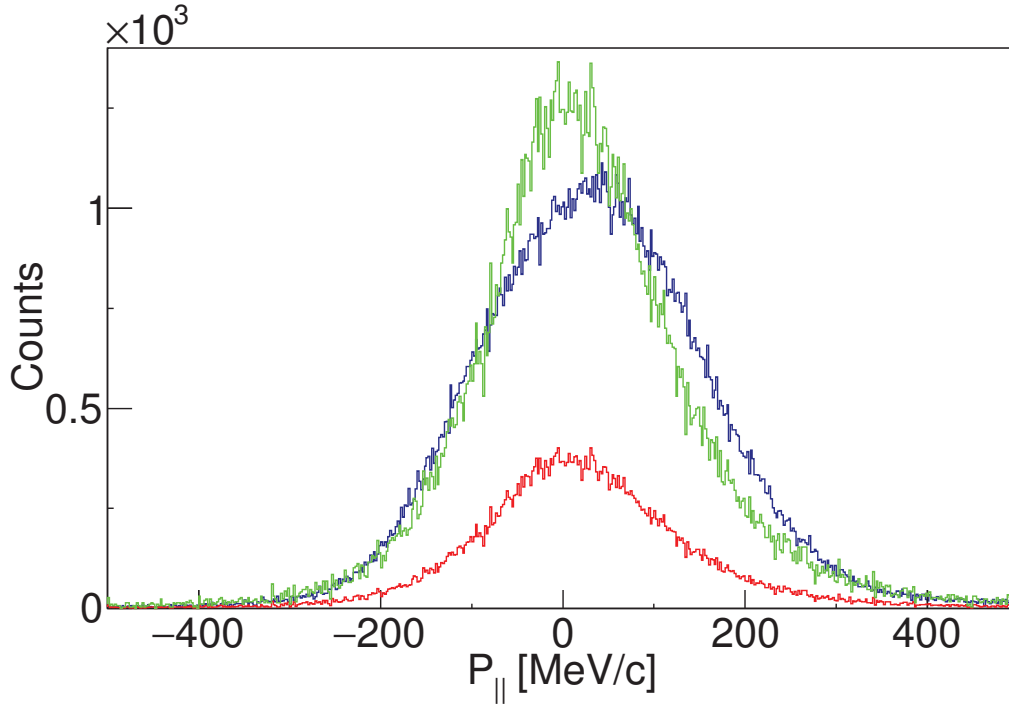


**Figure 4.10:** The longitudinal momentum distribution for two different intervals in the relative energy spectrum. Blue spectrum for  $E_{\text{fn}} = 0.4 \pm 0.2$  MeV and red spectrum for  $E_{\text{fn}} = 1.35 \pm 0.15$  MeV. The green spectrum is the same as the red, but scaled to the same number of events as in the blue spectrum for easier comparison.

peak in the relative energy spectrum origin from the knockout of a higher  $l$ -orbital neutron than the higher lying peak. Why the blue spectrum is shifted towards positive momenta is not understood though.

At this stage it is not possible to disentangle the spin and parity of the unbound states in  $^{29}\text{Ne}$ . One major question is how many resonances are present in the relative energy spectrum. By observing the number of counts in the peak at 0.4 MeV in the relative energy spectrum and comparing this with the number of counts in the peaks in the  $\gamma$ -spectrum, taking the efficiency and acceptance of DALI2 into account, the conclusion is that there are at least a factor of 5 more events in the relative energy peak than in the  $\gamma$ -peaks. This is one argument that the lower peak actually consists of more than one resonances, which has to be investigated further before any conclusions can be made. Once all resonances have been found, a level scheme can be constructed for  $^{29}\text{Ne}$ . This should also tell us if the  $7/2^-$  state is to be found in the unbound states observed in this work. Finally the results should also be compared with large-scale shell model calculations.





## Chapter 5

# Fragmentation Reaction Cross Sections of B and C Isotopes

Before performing an experiment it is important to estimate the chance of success. This is highly dependent on the number of wanted reactions which can be expected during the experiment, i.e. the statistics. To estimate this, it is crucial to know the reaction cross sections for the involved reactions. For the production of light radioactive beams it is mainly the fragmentation cross section which is important. The models used to calculate the yield of different ions is based on data from stable beams. As experiments move towards more and more exotic nuclei, fragmentation may have to be performed in two steps. The second step would then include fragmentation reactions of unstable nuclei, where the fragmentation cross sections are not as well known.

In Paper I, the one-proton  $x$ -neutron ( $1pxn$ ) removal reaction cross sections are measured for several boron and carbon isotopes. Even though these ions probably are too light for beam production, it is useful to compare their cross sections with existing models to investigate how well the models work for more exotic nuclei.

### 5.1 Experiment

The experiment was performed at GSI/FAIR, using the R<sup>3</sup>B/LAND-setup, described in Sec. 2.5.1 and 2.5.2. The experiment was a 10-day-long overview experiment, ranging from the proton to the neutron dripline for  $2 < Z < 10$  nuclei. With many different nuclei created and studied during the experiment, it has resulted in several publications, including Papers I, II, III, IV and V.

The radioactive beam was created from an <sup>40</sup>Ar beam, with a kinetic

energy of 490 MeV/nucleon, impinging on a beryllium target. The FRS was used to select the wanted isotopes among those produced in the reactions at the production target. To cover the wide range of isotopes in the experiment, six different settings of the FRS were used. Also several different secondary targets were used, including plastic, carbon and lead. For the cross section calculations, only data with the carbon target have been used.

### 5.2 Data Analysis

The cross section is calculated according to Eq. (2.6). The number of nuclei in the target is calculated from the areal densities of the target, which for the two different carbon targets used are 935 mg/cm<sup>2</sup> and 558 mg/cm<sup>2</sup>. From the experimental data the number of incoming and outgoing ions are needed. How the identification of the ions is done is described in Sec. 6.1. However, nuclear reactions may occur not only in the target but also in other materials in the beam line. As this also can contribute to the number of reactions, it has to be accounted for. This is done using data from so-called empty-target runs, where the target has been removed. In this way it is possible to measure how large the contribution from reactions which are happening in other materials than the target is.

The selection is done of one incoming boron or carbon isotope in the ranges  $^{10-15}\text{B}$  or  $^{10-18}\text{C}$ <sup>1</sup>. The number of events in this selection is the number of incoming ions. With this selection, further conditions are set on the outgoing fragment. One proton should be removed in the reaction together with  $x$  number of neutrons. The one-proton removal condition is set, using the energy loss as is shown in Fig. 5.1 (a). In (b) the different masses for the one-proton removal are shown. The number of outgoing fragments is then given by the number of events in each of the peaks in the mass spectrum. As mentioned above, this must also be compensated for the background contribution.

### 5.3 Results and Discussion

The determined cross sections are shown in Fig. 5.2 and 5.3 for carbon and boron isotopes, respectively. The results are compared to two different models, ABRABLA07 [30] and EPAX3 [55, 56]. The latter does not agree very well with the experimental data which is not surprising as it is limited to the mass region  $A = 40 - 209$ . The ABRABLA07 model is in surprisingly good agreement, though, at least after an adjustment to the model. The multiplication factor of the excitation energy per removed nucleon is decreased

---

<sup>1</sup>Except  $^{11}\text{C}$  where no data was available.

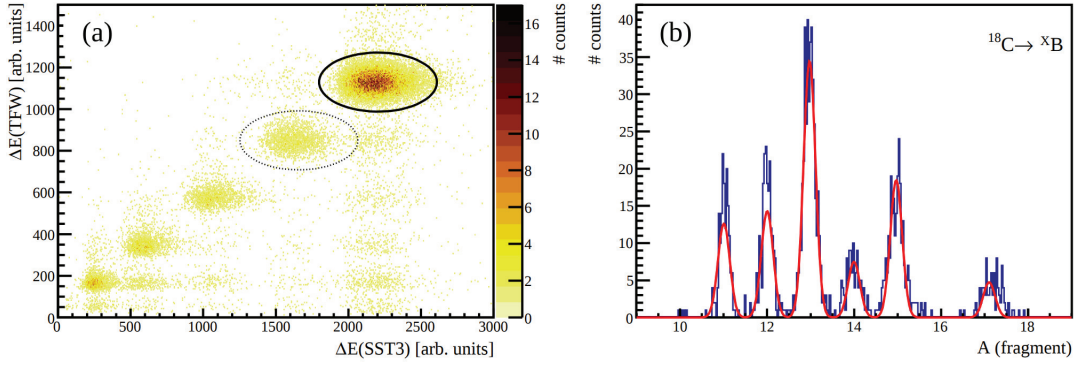


**Figure 5.1:** The charge (a) identification of outgoing fragments with incoming  $^{18}\text{C}$ . The solid black ellipse indicates the unreacted beam and the dashed ellipse one-proton removal. In (b), the mass identification of the fragments fulfilling the one-proton removal condition is shown. Figure from Paper I.

to 0.6 from the default value  $2^2$ . This value was determined by comparison of the experimental cross sections with the values given by the model using different multiplication factors. This value is used in the figures. For a more detailed description of how the multiplication factor was deduced, see Ref. [57]. A direct experimental determination of the excitation energy induced on average per abraded nucleon would be very desirable.

<sup>2</sup>The default value gives a pre-fragment excitation energy of 26.6 MeV per abraded nucleon.

## 5. Fragmentation Reaction Cross Sections of B and C Isotopes

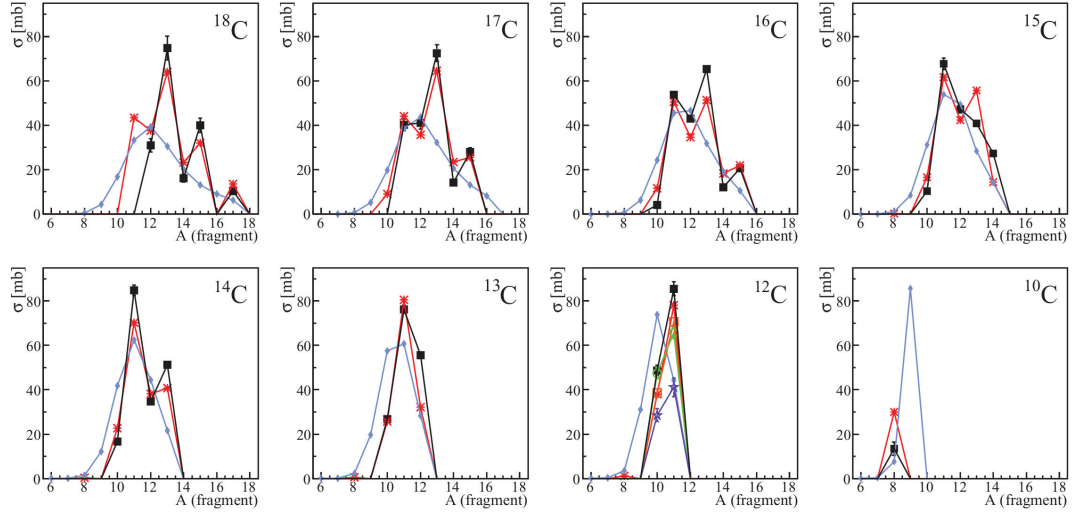


**Figure 5.2:** Measured cross sections for the one-proton  $x$ -neutron removal reaction from  $^{10-18}\text{C}$  isotopes (black squares). Two different models are used for comparison: ABRABLA07 [30] with multiplication factor 0.6 of the excitation energy per abraded nucleon (red stars) and EPAX3 [55, 56] (blue diamonds). Three other measurements are included for  $^{12}\text{C}$  on a C target: at 600 MeV/nucleon [58] (orange squares), at 250 MeV/nucleon [59] (green circles), and at 400 MeV/nucleon [60] (purple stars). Figure from Paper I.

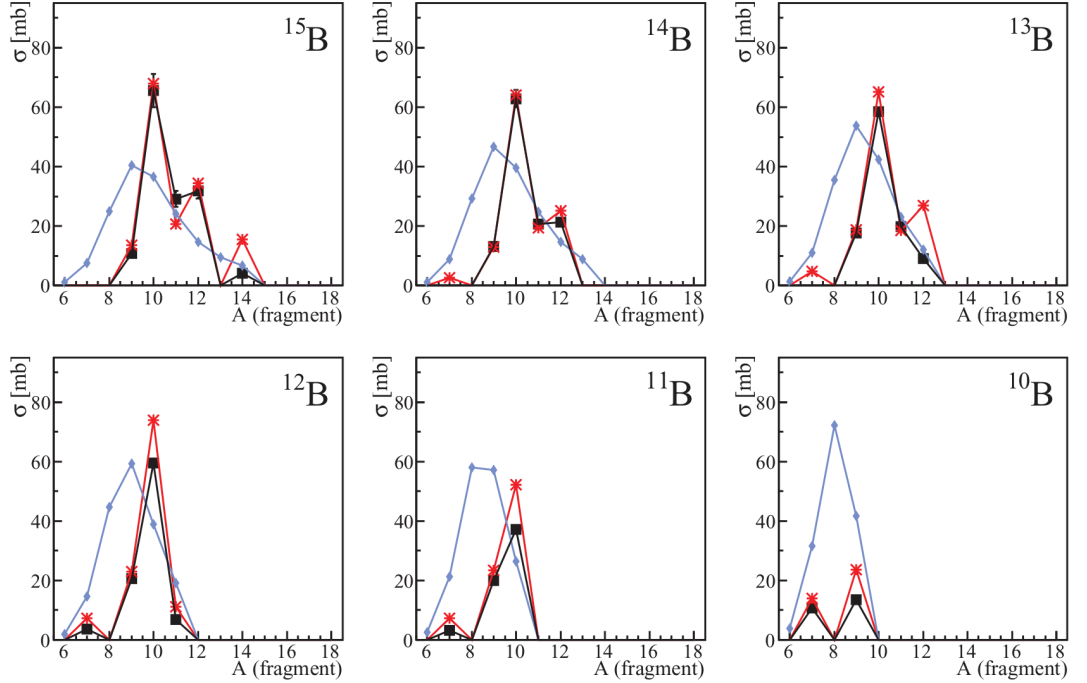


**Figure 5.3:** Measured cross sections for the one-proton  $x$ -neutron removal reaction from  $^{10-15}\text{B}$  isotopes (black squares). Two different models are used for comparison ABRABLA07 [30] with multiplication factor 0.6 of the excitation energy per abraded nucleon (red stars) and EPAX3 [55, 56] (blue diamonds). Figure from Paper I.

## Chapter 6

# Unbound States in Be and F

In Ch. 4 the results on unbound states in the one-neutron halo nucleus  $^{29}\text{Ne}$  were presented. In this chapter further studies on unbound states are presented, focusing on the unbound nucleus  $^{13}\text{Be}$  and unbound states in  $^{25,26}\text{F}$ .

The Be isotopes have drawn attention due to the interplay between the shell model and cluster structures in the nuclei. The ground state of  $^9\text{Be}$ , is expected to be a three body system consisting of  $\alpha + \alpha + n$ . When moving closer to the neutron drip line, the nucleus  $^{12}\text{Be}$  shows strong configuration mixing, breaking the shell closure at  $N=8$ . It has been shown that the ground state of  $^{12}\text{Be}$  consists of an admixture of closed  $p$ -shell and  $sd$ -shell configurations [14]. This also suggests that the wave function of the ground state of the unbound nucleus  $^{13}\text{Be}$  has a large  $sd$ -wave component. A theoretical study [61], suggests that in  $^{14}\text{Be}$ , the lowest  $(sd)^4$  state may be close to the lowest  $(sd)^2$  state, concluding that an admixture of an  $sd$ -component can be expected in the ground state of  $^{14}\text{Be}$ . For this question, the structure of  $^{13}\text{Be}$  can be used, as a large part of the wave function of its ground state then also would be of an  $sd$ -configuration.

There have been many experiments on  $^{13}\text{Be}$  trying to understand its nuclear structure [53, 62–66]. However, the results of these experiments are not in agreement. Especially when comparing the results for low-lying excited states the results differ between the two different experimental methods used: the missing mass method and the invariant mass method. In Paper II, the differences are studied and it concludes that they are caused by the missing  $\gamma$ -ray measurements in the invariant mass approaches.

The proton-neutron interaction can be studied using nuclei with doubly closed shells plus one neutron and one proton. This is the case for the  $^{26}\text{F}$  nucleus, consisting of an  $^{24}\text{O}$  core plus a  $\pi 0d_{5/2}$  proton and a  $\nu 0d_{3/2}$  neutron, which couple to a  $J^\pi = 1^+ - 4^+$  multiplet. The proximity to the neutron dripline makes  $^{26}\text{F}$  a very good case to study the influence of the continuum on the proton-neutron interaction. So far, measurements of

the excitation energy of the bound  $J^\pi = 1^+, 2^+$  and  $4^+$  states have been performed [67–69]. In Paper III, the unbound  $J^\pi = 3^+$  state is measured to complete the measurements on the multiplet. Both the unbound  $^{13}\text{Be}$  and the unbound states in  $^{26}\text{F}$  were measured during the same experiment as the measurements on the fragmentation cross sections, described in Ch. 5.

## 6.1 Data Analysis

All incoming ions are identified on an event-by-event basis, in a similar way as described in Sec. 4.2. The ToF is measured between the FRS and the POS detector, which together with the well-defined flight-path length in the fragment separator can be used to calculate the velocity of the ion. The charge is given by the energy loss in the POS detector. To minimise the number of misidentifications, also the energy loss in the SST detectors are used to calculate the charge. The SST detectors also measure the track, giving the hit position at the target.

Behind the target, another set of SST detectors identify the charge of the outgoing fragments, again based on the energy loss in the detectors. Since there is a significant amount of material in the beam-line from the target to the TFW, a second charge identification is done at the TFW to discriminate events where reactions have occurred between the target and the TFW. The principle of the mass identification is the same as for the incoming ions, with the difference that the flight-path length is not as well defined in the magnet because of its large acceptance. The ToF is measured between the POS and the TFW detectors and the SST and GFI detectors track the ions before and after ALADIN.

The length of the flight path depends on the magnetic rigidity of the outgoing fragment, as it influences the deflection in the magnet. The magnetic rigidity depends both on the mass and velocity of the fragment, according to Eq. (2.7). Since the velocity is measured using the ToF and the flight path distance also this depends on the magnetic rigidity. This results in an equation system where all parameters depend on each other, which is solved in an iterative way. Using also the tracking information of the SST and GFI detectors, it becomes an over-determined system where the squared sum of all the relative errors is minimised. Once this problem is solved, the mass-over-charge of the fragment is determined.

With the incoming and outgoing identification, the desired reaction channel can be selected. The unbound  $^{13}\text{Be}$  nucleus was studied in one-proton knockout reactions from  $^{14}\text{B}$  resulting in the unbound system  $^{12}\text{Be}+n$ . The unbound states in  $^{26}\text{F}$  were also studied in one-proton knockout reactions, from  $^{27}\text{Ne}$ . Hence, the reaction channels which should be studied are the incoming  $^{14}\text{B}$  or  $^{27}\text{Ne}$  together with an outgoing  $^{12}\text{Be}$  or  $^{26}\text{F}$  in coincidence with one neutron in LAND. In addition, a condition was set in the Crystal

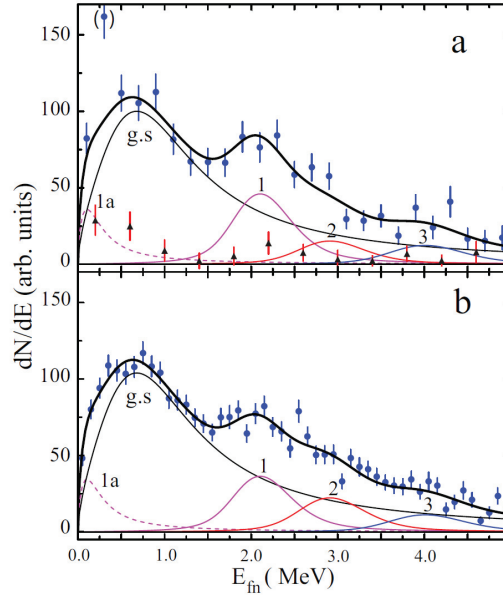


**Figure 6.1:** The relative energy spectrum of  $^{12}\text{Be}+n$  obtained in proton knockout from  $^{14}\text{B}$  at 400 MeV/nucleon (a), and 35 MeV/nucleon (b, from Ref. [65]). Contributions from  $^{12}\text{Be}+n+\gamma$  are indicated by ( $\blacktriangle$ ). The pink, red and blue curves are Breit-Wigner fits to three resonances and the dashed line is their decay branches to the  $\gamma$ -decaying  $^{12}\text{Be}(2^+)$  state. The point in parenthesis in (a) was excluded from the fit. Figure from Paper II.

Ball to detect at least one proton.

## 6.2 Results and Discussion

The results for the unbound  $^{13}\text{Be}$  are obtained in the same way as for  $^{29}\text{Ne}$  in Sec. 4.4. The relative energy spectrum including the Doppler-corrected  $\gamma$ -energies is shown in Fig. 6.1. Three resonances are identified in the spectrum and are fitted with three Breit-Wigner functions (pink, red and blue curves). Because of the rather wide and overlapping functions the peak positions of peak 2 and 3 were fixed as well as the width of peaks 1, 2 and 3. The parameters for these curves were taken from the missing-mass experiments [62–64]. Comparing the data of the two different experiments, one-proton knockout at 400 MeV/nucleon (a) and one-proton knockout at 35 MeV/nucleon (b), it can be concluded that the reaction mechanism is independent of the energy and target. In Tab. 6.1 a summary of the resonance positions and widths are presented.

The resonance energy of the first peak is in agreement with the missing-mass experiments. The interpretation of these results is that the first  $5/2^+$  state can decay either directly to the ground state in  $^{12}\text{Be}$  or via the first excited state in  $^{12}\text{Be}$  (indicated by peak 1a) followed by  $\gamma$ -decay to the



**Table 6.1:** Resonance energies ( $E_r$ ), widths ( $\Gamma$ ) and associated spins and parities ( $I^\pi$ ) for the  $^{13}\text{Be}$  isotope. Fixed parameters are indicated with (\*).

Peak	$E_r$	$\Gamma$	$I^\pi$
g.s.	0.86(4)	1.70(15)	$1/2^+$
1a	0.1	-	$5/2_1^+$
1	2.11(5)	0.4*	$5/2_1^+$
2	2.92*	0.4*	$5/2_2^+$
3	4.0*	0.4*	$(3/2^+)$

ground state. The same thing is true also for the assumed  $3/2^+$  state. This feeding is probably also the reason for the disagreement between the different experiments and shows the problems of drawing conclusions from spectra of relative energy without access to  $\gamma$ -detection.

For the unbound states in  $^{26}\text{F}$ , no  $\gamma$ -decay was found in coincidence with the  $^{25}\text{F}+n$  system, indicating that all excited states in  $^{26}\text{F}$  decay directly to the ground state of  $^{25}\text{F}$ . As the neutron is expected to occupy the  $\nu 0d_{3/2}$  orbital, the orbital angular momentum is  $l = 2$ . This affects the shape of the Breit-Wigner resonance and hence Eq. (4.3) has to be modified to

$$f(E) = \frac{\Gamma_l}{(E - \Delta_l - E_r)^2 + \Gamma_l^2/4}, \quad (6.1)$$

with the apparent width

$$\Gamma_l = \Gamma \frac{P_l(E)}{P_l(E_r)}, \quad (6.2)$$

and the energy shift

$$\Delta_l = \Gamma \frac{S_l(E_r) - S_l(E)}{2P_l(E_r)}. \quad (6.3)$$

$P_l$  and  $S_l$  are the penetrability and shift functions, respectively. With this form of the Breit-Wigner function, two peaks are fitted in Fig. 6.2. Two different fits are made, (a) with  $\Delta_l$  calculated as in Eq. (6.3) and (b) with  $\Delta_l = 0$ . As can be seen in the figure, the difference between the two cases is small. In Tab. 6.2 a summary of the resonance energies ( $E_r$ ), widths ( $\Gamma$ ) and excitation energies ( $E^*$ ) are listed, with the neutron separation energy  $S_n = 1071(130)$  keV [70]. Also the calculated single-particle resonance widths for different angular momenta ( $\Gamma_{sp}^{l=0,1,2}$ ) are listed for comparison.

The second peak is broad and also has a very large uncertainty, which makes it hard to conclude which angular momentum is the most probable. It is possible that it consists of several overlapping resonances, but this assumption is hard to confirm or reject from the present data. Comparing the measured width of the first resonance with the calculated widths, one can see that it is compatible with both  $l = 1$  and  $l = 2$ . In a previous experiment [71], using nucleon-exchange reactions  $^{26}\text{Ne} \rightarrow ^{26}\text{F}$ , a resonance at



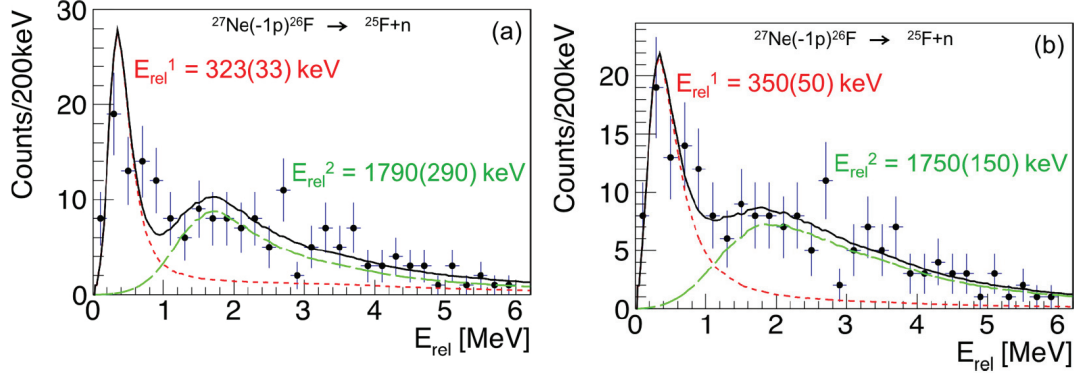


**Figure 6.2:** The relative energy spectrum of  $^{26}\text{F}$  with two Breit-Wigner  $l = 2$  resonance fits (dashed red and green). The black line is the sum of both resonances. In (a) the energy shift  $\Gamma_l$  is calculated according to Eq. (6.3), and in (b) it is 0. The values given are the resonance peak positions. Figure from Paper III.

**Table 6.2:** The resonance energies, widths and excitation energies of the two resonances found in Fig. 6.2. The calculated width of single-particle states with three different angular momenta  $l = 0, 1, 2$  are given for comparison. All energies are given in keV.

Peak	$E_r$	$\Gamma$	$E^*$	$\Gamma_{sp}^{l=0}$	$\Gamma_{sp}^{l=1}$	$\Gamma_{sp}^{l=2}$
1	323(33)	570(480)	1394(134)	3080	1038	74
2	1790(290)	4200(2500)	2861(318)	7941	6127	2966

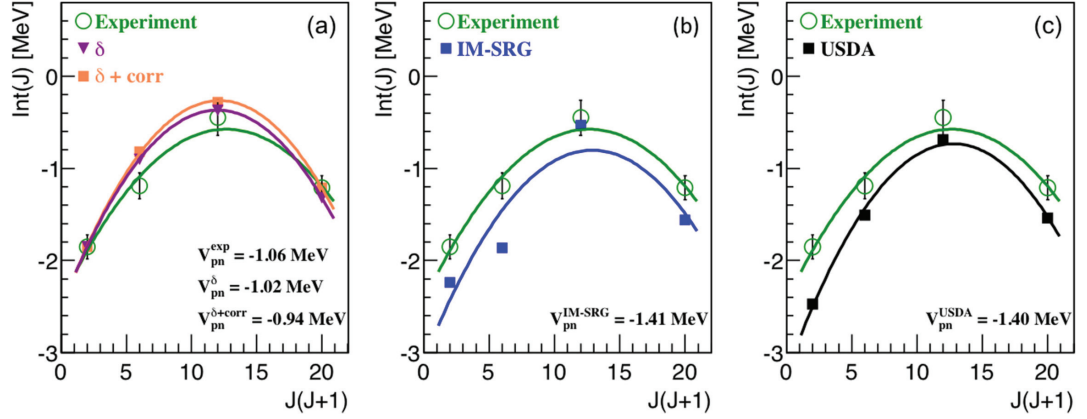


**Figure 6.3:** The interaction energy  $\text{Int}(J)$  as a function of the total angular momentum  $J$  for  $^{26}\text{F}$ . Three different models are used for comparison, in (a) a  $\delta$  interaction both with and without  $J$ -dependent radial corrections, in (b) the IM-SRG procedure and in (c) the USDA interaction. Also the monopole values  $V_{pn}$  are given. Figure from Paper III.

271(37) keV was observed. As this reaction would convert a  $\pi 0d_{5/2}$  proton into a  $\nu 0d_{3/2}$  neutron it should produce all  $J^\pi = 1^+ - 4^+$  states. A knockout reaction of a  $\pi 0d_{5/2}$  proton from  $^{27}\text{Ne}$  would produce the same configurations. Since both experiments find the same resonance, it is reasonable to assume that it constitutes the  $J^\pi = 3^+$  state and hence that the angular momentum is  $l = 2$ .

This information can be used to calculate the interaction energy,  $\text{Int}(J)$ , following the same approach as in [68], as

$$\text{Int}(J) = \text{BE}(^{26}\text{F}_J) - \text{BE}(^{26}\text{F}_{\text{free}}), \quad (6.4)$$

with

$$\text{BE}(^{26}\text{F}_{\text{free}}) = \text{BE}(^{25}\text{F}) + \text{BE}(^{25}\text{O}) - \text{BE}(^{24}\text{O}), \quad (6.5)$$

where BE is the binding energy of the given nucleus and  $\text{BE}(^{26}\text{F}_J)$  is the energy of a given  $J^\pi$  state. With values of  $\text{Int}(1,2,4)$  from Ref. [68] and the value of  $\text{Int}(3) = -0.45(19)$  MeV obtained in Paper III, it is plotted in Fig. 6.3. This result is compared with several different model calculations. Both the shell-model calculation using the USDA interaction and *ab initio* valence-space IM-SRG calculations show an overall good agreement with the experimental data. There is however a difference in the monopole interaction between the models and the experimental data. This could be interpreted as an effect of the proximity of the continuum.

## Chapter 7

# Coulomb Dissociation and Neutron Capture Rates

As discussed in Sec. 1.2, the r-process is responsible for the creation of almost half of all nuclei heavier than nickel in the Universe. Despite its importance, it is still the nucleosynthesis process which we know the least about. One of the reasons is that it is a large reaction network containing isotopes which are often not well-studied or even not yet produced in the laboratory. As small deviations in the early parts of the network can cause large deviations later on, it is important to know the properties of the nuclei involved in the chain. Especially the neutron capture cross section is of importance and that is what is measured via Coulomb dissociation in Papers IV and V.

The experiment is similar to those in Papers I, II and III. The reactions studied in Paper IV are  $^{20,21}\text{N}(\gamma, n)^{19,20}\text{N}$  and in Paper V  $^{18}\text{C}(\gamma, n)^{17}\text{C}$ . In both, data for a lead target is analysed, and the time-reversed neutron-capture reaction  $(\gamma, n)$  is studied via Coulomb dissociation.

### 7.1 Data Analysis

The method of identification of the incoming and outgoing fragments is the same as described in Sec. 6.1. Coulomb dissociation reactions are identified by selecting incoming  $^{18}\text{C}$  ( $^{21,22}\text{N}$ ) ions and outgoing  $^{17}\text{C}$  ( $^{20,21}\text{N}$ ) in coincidence with one neutron and  $\gamma$ -photons. There may also be contributions to these events from nuclear reactions and reactions in other parts of the beam line. To subtract this background, the same reaction channels were studied using a carbon target and an empty target. The reaction probability in the carbon target can be scaled to account for the nuclear reaction contributions and the empty target allows to subtract the reactions occurring in other parts of the setup.

By studying the Doppler-corrected  $\gamma$ -energy spectrum measured in the Crystal Ball it is possible to conclude which excited states have been popu-

**Table 7.1:** Coulomb dissociation cross sections for three different isotopes of C and N. The uncertainties listed are only the statistical errors.

Isotope	State	$\sigma_{CD}$ [mb]
$^{18}\text{C}$	g.s.	$32 \pm 13$
	1st exc.	$40 \pm 8$
	2nd exc.	$43 \pm 6$
	total	$115 \pm 8$
$^{20}\text{N}$	g.s.	$15 \pm 16$
	1st exc.	$36 \pm 6$
	total	$90 \pm 12$
$^{21}\text{N}$	g.s.	$31 \pm 16$
	1st+2nd exc.	$47 \pm 8$
	total	$75 \pm 13$

lated in the reactions. With this identification it is possible to also investigate the reaction cross section leading to the different excitation energies in the daughter nuclei.

## 7.2 Results and Discussion

The measured cross sections for the Coulomb dissociation of  $^{18}\text{C}$  and  $^{20,21}\text{N}$  are presented in Tab. 7.1. The cross sections for the population of the ground state as well as the first excited states are listed together with the total cross sections. For  $^{21}\text{N}$  the two first excited states could not be resolved, hence the total cross section of the two first excited states is given in the table.

The Coulomb dissociation cross sections can then be used to calculate the neutron capture cross sections ( $\sigma_{n,\gamma}$ ) using the principle of detailed balance and the virtual photon theory, giving

$$\sigma_{n,\gamma} = \frac{2(2I_i + 1)}{(2I_f + 1)(2I_n + 1)} \frac{k_\gamma^2}{k_{c.m.}^2} \frac{d\sigma_{CD}}{dE^*} \frac{1}{n_{E1}(E^*)} E^* \quad (7.1)$$

where  $I$  is the total angular momentum with indices  $i$  for incoming ion,  $f$  for outgoing fragment and  $n$  for the neutron ( $I_n=1/2$ ),  $k$  is the momentum of the photon and  $k_{c.m.}$  the relative motion of the fragment and emitted neutron,  $\sigma_{CD}$  is the Coulomb dissociation cross section,  $E^*$  is the excitation energy and  $n_{E1}$  is the number of virtual E1-photons.

The reaction rate for neutron-capture can be calculated as a function of the temperature. In Fig. 7.1 this is shown for  $^{19}\text{N}$  (solid black line). In the same figure a theoretical curve (dashed black line) is calculated from Ref. [72]. It is clear that the model and the experimental data do not agree, hence an update of the model is needed to reflect the measured neutron

capture rate. It is also clear that neutron capture from excited states does not contribute to the total capture rate at  $T < 3$  GK.

As mentioned earlier, the neutron capture rate is an important factor for models of the r-process. It turns out that when updating the neutron capture rates according to the results obtained for  $^{19,20}\text{N}$  and using one such model [73], that the final abundance of  $^{19}\text{F}$  was decreased by 10%. Higher mass nuclei were unaffected though.

Also the neutron capture rate of  $^{17}\text{C}$  showed a large deviation from theoretical calculations. In this case a change of the neutron capture rate did not have any affect on the final abundances using the r-process model.

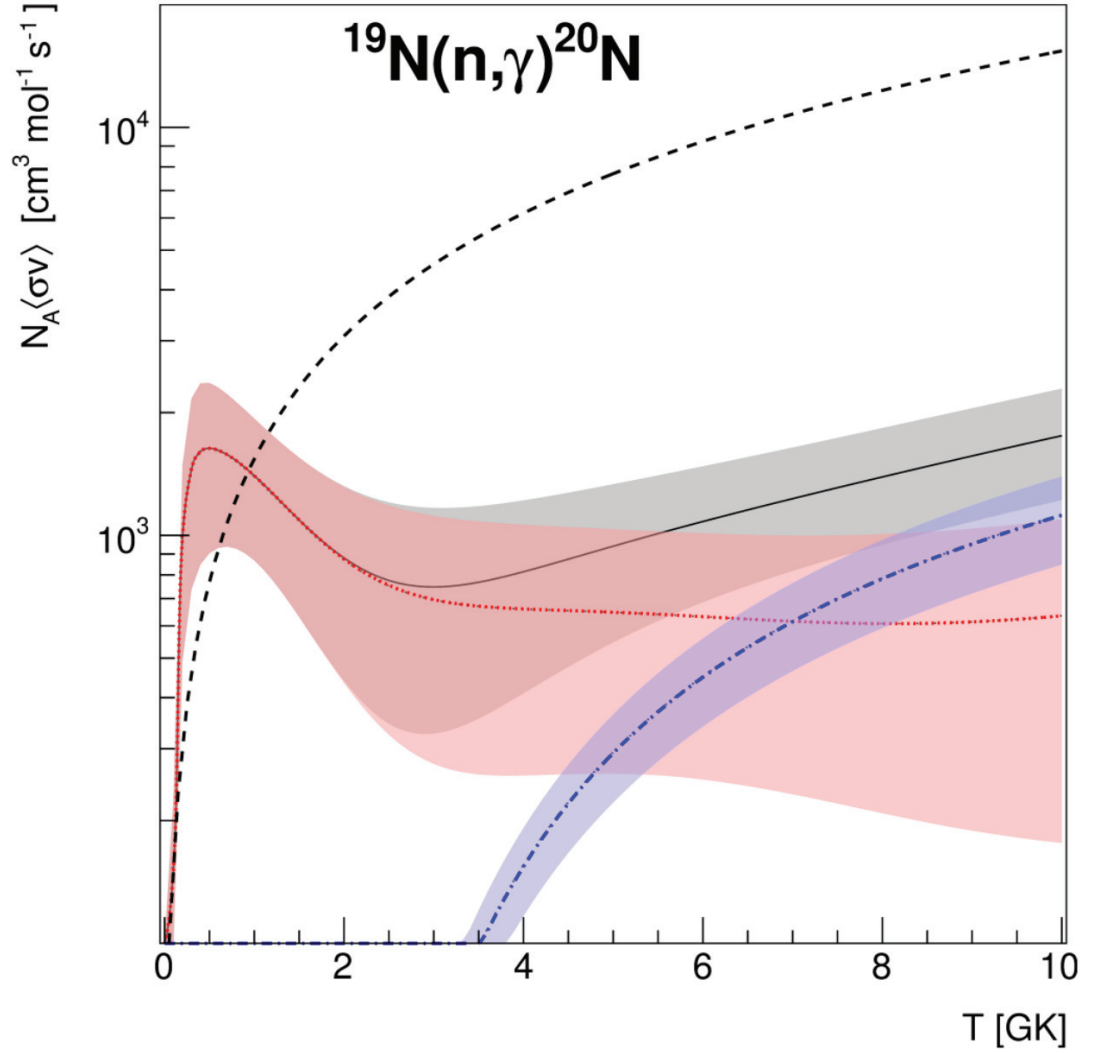


**Figure 7.1:** The neutron capture rate of  $^{19}\text{N}$ , black solid line. The contribution from the ground state is indicated with the red dotted line and from the first two excited states with the blue dashed-dotted line. The shaded areas indicate the errors. The black dashed line is calculated from a theoretical model [72]. Figure from Paper IV.

# Chapter 8

## Summary

In Ch. 4, results on the first measurements of unbound states in  $^{29}\text{Ne}$  are reported. The number of states and their spin and parity assignment are still under investigation, but based on the fit of Breit-Wigner functions to the relative energy spectrum, and the number of events in the peaks in the relative energy spectrum compared to the  $\gamma$ -spectrum, there seem to be three different states. Two of the resonances are present in the lower-energy peak around 0.4 MeV in the relative energy spectrum, while the third resonance is found at 1.3 MeV. The detection of the lowest resonance in coincidence with  $\gamma$ -rays indicates that this state decays to excited states in  $^{28}\text{Ne}$ , while the other two resonances decay to the ground state. Assuming there are two resonances in the lower peak, at least one of these should have a larger angular momentum than the resonance at 1.3 MeV and may even be a candidate for  $7/2^-$  state. This is based on the longitudinal momentum distributions for the different relative energy peaks, where a wider spread of the momentum is shown for events with the lower energy resonance. The  $\gamma$ -rays are in coincidence with the lowest of the three resonances as well as with a wider spread in the longitudinal angular momentum, indicating that at least this resonance has a larger angular momentum.

The analysis is still ongoing, and it is especially the fitting of the relative energy spectrum which needs to be improved. The main question is how many resonances are present in the peaks shown in the relative energy spectrum and what are the spin and parities of the corresponding excited states. Once concluded, the results should also be compared to large-scale shell model calculations.

In Paper I, the experimental one-proton  $x$ -neutron removal cross sections were measured for 6 different boron isotopes and 8 different carbon isotopes. The results were compared with two different models, ABRABLA07 and EPAX3. After decreasing the excitation energy per removed nucleon in the ABRABLA07 model, the agreement with the experimental data turns out to be surprisingly good .

The unbound nucleus  $^{13}\text{Be}$  was studied in Paper II. Three different resonances were found in the relative energy spectrum, at 2.11, 2.92 and 4.00 MeV. Each of these resonances may decay to the ground state of  $^{12}\text{Be}$ , but from  $\gamma$ -ray coincidence measurements it was concluded that both the resonance at 2.11 and 4.00 MeV also decay via the first excited state in  $^{12}\text{Be}$ . These results show the importance of taking possible population of excited states in the daughter nucleus into account when evaluating relative energy spectra, as this turned out to be the cause of disagreement between results from previous measurements of  $^{13}\text{Be}$ .

In Paper III, unbound states in  $^{26}\text{F}$  were measured. In this case no  $\gamma$ -rays were detected in coincidence, hence all unbound states decayed directly to the ground state in  $^{25}\text{F}$ . In the relative energy spectrum, two resonances were found at 0.32 MeV and at 1.79 MeV. The lower of the two resonances was assigned to the  $J^\pi=3^+$  state which is part of the  $J^\pi = 1^+ - 4^+$  multiplet and was the last state in the multiplet to be observed. This was used to calculate the interaction energy for all the four states in the multiplet. The results show good agreement both with shell model calculations and *ab initio* valence-space IM-SRG calculations, but the lower multipole interaction in the experimental data compared to the model suggests that the proximity of the continuum may affect the effective proton-neutron interaction.

Papers IV and V reported on the Coulomb dissociation cross sections of  $^{20,21}\text{N}$  and  $^{18}\text{C}$ . The results were used to extract the neutron capture cross sections of  $^{19,20}\text{N}$  and  $^{17}\text{C}$ , using the principle of detailed balance and the virtual photon theory. The neutron capture cross sections were used in model calculations of the r-process nucleosynthesis. The measured neutron capture cross section of  $^{19}\text{N}$  was up to a factor of 5 higher than the one previously used in the calculations. The increase of the cross section led to a 10 percent decrease in the final fluorine abundances.



# Bibliography

- [1] O. Haxel, J. H. D. Jensen, and H. E. Suess, “On the ”magic numbers” in nuclear structure,” *Phys. Rev.*, vol. 75, pp. 1766–1766, Jun 1949.
- [2] M. G. Mayer, “On closed shells in nuclei. II,” *Phys. Rev.*, vol. 75, pp. 1969–1970, Jun 1949.
- [3] R. Casten, *Nuclear Structure from a Simple Perspective*. Oxford University Press, 2001.
- [4] I. Tanihata, H. Hamagaki, O. Hashimoto, Y. Shida, N. Yoshikawa, K. Sugimoto, O. Yamakawa, T. Kobayashi, and N. Takahashi, “Measurements of interaction cross sections and nuclear radii in the light  $p$ -shell region,” *Phys. Rev. Lett.*, vol. 55, pp. 2676–2679, Dec 1985.
- [5] P. G. Hansen and B. Jonson, “The neutron halo of extremely neutron-rich nuclei,” *EPL (Europhysics Letters)*, vol. 4, no. 4, p. 409, 1987.
- [6] B. Jonson, “Light dripline nuclei,” *Physics Reports*, vol. 389, no. 1, pp. 1 – 59, 2004.
- [7] T. Nakamura, N. Kobayashi, Y. Kondo, Y. Satou, N. Aoi, H. Baba, S. Deguchi, N. Fukuda, J. Gibelin, N. Inabe, M. Ishihara, D. Kameda, Y. Kawada, T. Kubo, K. Kusaka, A. Mengoni, T. Motobayashi, T. Ohnishi, M. Ohtake, N. A. Orr, H. Otsu, T. Otsuka, A. Saito, H. Sakurai, S. Shimoura, T. Sumikama, H. Takeda, E. Takeshita, M. Takechi, S. Takeuchi, K. Tanaka, K. N. Tanaka, N. Tanaka, Y. Togano, Y. Utsuno, K. Yoneda, A. Yoshida, and K. Yoshida, “Halo structure of the island of inversion nucleus  $^{31}\text{Ne}$ ,” *Phys. Rev. Lett.*, vol. 103, p. 262501, Dec 2009.
- [8] M. Takechi, T. Ohtsubo, M. Fukuda, D. Nishimura, T. Kuboki, T. Suzuki, T. Yamaguchi, A. Ozawa, T. Moriguchi, H. Ooishi, D. Nagae, H. Suzuki, S. Suzuki, T. Izumikawa, T. Sumikama, M. Ishihara, H. Geissel, N. Aoi, R.-J. Chen, D.-Q. Fang, N. Fukuda, I. Hachiuma, N. Inabe, Y. Ishibashi, Y. Ito, D. Kameda, T. Kubo, K. Kusaka, M. Lantz, Y.-G. Ma, K. Matsuta, M. Mihara, Y. Miyashita, S. Momota, K. Nami-hira, M. Nagashima, Y. Ohkuma, T. Ohnishi, M. Ohtake, K. Ogawa,

- H. Sakurai, Y. Shimbara, T. Suda, H. Takeda, S. Takeuchi, K. Tanaka, R. Watanabe, M. Winkler, Y. Yanagisawa, Y. Yasuda, K. Yoshinaga, A. Yoshida, and K. Yoshida, “Interaction cross sections for Ne isotopes towards the island of inversion and halo structures of  $^{29}\text{Ne}$  and  $^{31}\text{Ne}$ ,” *Physics Letters B*, vol. 707, no. 3, pp. 357 – 361, 2012.
- [9] N. Kobayashi, T. Nakamura, Y. Kondo, J. A. Tostevin, Y. Utsuno, N. Aoi, H. Baba, R. Barthelemy, M. A. Famiano, N. Fukuda, N. Inabe, M. Ishihara, R. Kanungo, S. Kim, T. Kubo, G. S. Lee, H. S. Lee, M. Matsushita, T. Motobayashi, T. Ohnishi, N. A. Orr, H. Otsu, T. Otsuka, T. Sako, H. Sakurai, Y. Satou, T. Sumikama, H. Takeda, S. Takeuchi, R. Tanaka, Y. Togano, and K. Yoneda, “Observation of a  $p$ -wave one-neutron halo configuration in  $^{37}\text{Mg}$ ,” *Phys. Rev. Lett.*, vol. 112, p. 242501, Jun 2014.
- [10] E. K. Warburton, J. A. Becker, and B. A. Brown, “Mass systematics for  $A=29\text{--}44$  nuclei: The deformed  $A\sim 32$  region,” *Phys. Rev. C*, vol. 41, pp. 1147–1166, Mar 1990.
- [11] X. Campi, H. Flocard, A. Kerman, and S. Koonin, “Shape transition in the neutron rich sodium isotopes,” *Nuclear Physics A*, vol. 251, no. 2, pp. 193 – 205, 1975.
- [12] K. Heyde and J. L. Wood, “Shape coexistence in atomic nuclei,” *Rev. Mod. Phys.*, vol. 83, pp. 1467–1521, Nov 2011.
- [13] A. Gade and S. N. Liddick, “Shape coexistence in neutron-rich nuclei,” *Journal of Physics G: Nuclear and Particle Physics*, vol. 43, no. 2, p. 024001, 2016.
- [14] A. Navin, D. W. Anthony, T. Aumann, T. Baumann, D. Bazin, Y. Blumenfeld, B. A. Brown, T. Glasmacher, P. G. Hansen, R. W. Ibbotson, P. A. Lofy, V. Maddalena, K. Miller, T. Nakamura, B. V. Pritychenko, B. M. Sherrill, E. Spears, M. Steiner, J. A. Tostevin, J. Yurkon, and A. Wagner, “Direct evidence for the breakdown of the  $N = 8$  shell closure in  $^{12}\text{Be}$ ,” *Phys. Rev. Lett.*, vol. 85, pp. 266–269, Jul 2000.
- [15] G. Steigman, “Primordial nucleosynthesis in the precision cosmology era,” *Annual Review of Nuclear and Particle Science*, vol. 57, no. 1, pp. 463–491, 2007.
- [16] B. D. Fields and K. A. Olive, “Big bang nucleosynthesis,” *Nuclear Physics A*, vol. 777, pp. 208 – 225, 2006. Special Issue on Nuclear Astrophysics.
- [17] S. Burles, K. M. Nollett, and M. S. Turner, “Big-bang nucleosynthesis: Linking inner space and outer space,” *ArXiv Astrophysics e-prints*, March 1999.

- 
- [18] C. Iliadis, *Nuclear Physics of Stars*. Wiley-VCH Verlag GmbH & Co. KGaA, 2nd ed., 2015.
- [19] M. Mumpower, R. Surman, G. McLaughlin, and A. Aprahamian, “The impact of individual nuclear properties on r-process nucleosynthesis,” *Progress in Particle and Nuclear Physics*, vol. 86, pp. 86 – 126, 2016.
- [20] F. Käppeler, R. Gallino, S. Bisterzo, and W. Aoki, “The *s*-process: Nuclear physics, stellar models, and observations,” *Rev. Mod. Phys.*, vol. 83, pp. 157–193, Apr 2011.
- [21] M. Arnould and S. Goriely, “The p-process of stellar nucleosynthesis: astrophysics and nuclear physics status,” *Physics Reports*, vol. 384, no. 1, pp. 1 – 84, 2003.
- [22] B. P. Abbott, R. Abbott, T. D. Abbott, F. Acernese, K. Ackley, C. Adams, *et al.*, “Multi-messenger observations of a binary neutron star merger,” *The Astrophysical Journal Letters*, vol. 848, no. 2, p. L12, 2017.
- [23] D. Kasen, B. Metzger, J. Barnes, E. Quataert, and E. Ramirez-Ruiz, “Origin of the heavy elements in binary neutron-star mergers from a gravitational-wave event,” *Nature*, vol. 551, pp. 80–84, 2017.
- [24] J. J. Cowan and W. K. Rose, “Production of C-14 and neutrons in red giants,” *Astrophysical Journal*, vol. 212, no. 1, pp. 149–158, 1977.
- [25] P. Denissenkov, G. Perdikakis, F. Herwig, H. Schatz, C. Ritter, M. Pig-natari, S. Jones, S. Nikas, and A. Spyrou, “The impact of (n, $\gamma$ ) reaction rate uncertainties of unstable isotopes near N=50 on the i-process nucleosynthesis in He-shell flash white dwarfs,” *Journal of Physics G: Nuclear and Particle Physics*, vol. 45, no. 5, p. 055203, 2018.
- [26] Y. Blumenfeld, T. Nilsson, and P. V. Duppen, “Facilities and methods for radioactive ion beam production,” *Physica Scripta*, vol. 2013, no. T152, p. 014023, 2013.
- [27] H. Simon, “Halo nuclei, stepping stones across the drip-lines,” *Physica Scripta*, vol. 2013, no. T152, p. 014024, 2013.
- [28] P. Díaz Fernández, H. Alvarez-Pol, R. Crespo, E. Cravo, L. Atar, A. Deltuva, T. Aumann, V. Avdeichikov, S. Beceiro-Novo, D. Bemmerer, J. Benlliure, C. A. Bertulani, J. M. Boillos, K. Boretzky, M. J. G. Borge, M. Caamaño, P. Cabanelas, C. Caesar, E. Casarejos, W. Catford, J. Cederkäll, M. Chartier, L. V. Chulkov, D. Cortina-Gil, U. Datta Pramanik, I. Dillmann, Z. Elekes, J. Enders, O. Ershova, A. Estradé, F. Farinon, B. Fernández-Domínguez, L. M. Fraile,

- M. Freer, D. Galaviz, H. Geissel, R. Gernhäuser, P. Golubev, K. Göbel, J. Hagdahl, T. Heftrich, M. Heil, M. Heine, A. Heinz, A. Henriques, M. Holl, A. Hufnagel, A. Ignatov, H. T. Johansson, B. Jonson, D. Jurčiukonis, N. Kalantar-Nayestanaki, R. Kanungo, A. Kelic-Heil, A. Knyazev, T. Kröll, N. Kurz, M. Labiche, C. Langer, T. Le Bleis, R. Lemmon, S. Lindberg, J. Machado, J. Marganec, A. M. Moro, A. Movsesyan, E. Nacher, A. Najafi, E. Nikolskii, T. Nilsson, C. Nociforo, V. Panin, S. Paschalis, A. Perea, M. Petri, B. Pietras, S. Pietri, R. Plag, R. Reifarth, G. Ribeiro, C. Rigollet, D. Rossi, M. Röder, D. Savran, H. Scheit, H. Simon, O. Sorlin, I. Syndikus, J. T. Taylor, O. Tengblad, R. Thies, Y. Togano, M. Vandebrouck, P. Velho, V. Volkov, A. Wagner, F. Wamers, H. Weick, C. Wheldon, G. Wilson, J. S. Winfield, P. Woods, D. Yakorev, M. Zhukov, A. Zilges, and K. Zuber, “Quasifree  $(p, pn)$  scattering of light neutron-rich nuclei near  $N = 14$ ,” *Phys. Rev. C*, vol. 97, p. 024311, Feb 2018.
- [29] L. Atar, S. Paschalis, C. Barbieri, C. A. Bertulani, P. Díaz Fernández, M. Holl, M. A. Najafi, V. Panin, H. Alvarez-Pol, T. Aumann, V. Avdeichikov, S. Beceiro-Novo, D. Bemmerer, J. Benlliure, J. M. Boillos, K. Boretzky, M. J. G. Borge, M. Caamaño, C. Caesar, E. Casarejos, W. Catford, J. Cederkall, M. Chartier, L. Chulkov, D. Cortina-Gil, E. Cravo, R. Crespo, I. Dillmann, Z. Elekes, J. Enders, O. Ershova, A. Estrade, F. Farinon, L. M. Fraile, M. Freer, D. Galaviz Redondo, H. Geissel, R. Gernhäuser, P. Golubev, K. Göbel, J. Hagdahl, T. Heftrich, M. Heil, M. Heine, A. Heinz, A. Henriques, A. Hufnagel, A. Ignatov, H. T. Johansson, B. Jonson, J. Kahlbow, N. Kalantar-Nayestanaki, R. Kanungo, A. Kelic-Heil, A. Knyazev, T. Kröll, N. Kurz, M. Labiche, C. Langer, T. Le Bleis, R. Lemmon, S. Lindberg, J. Machado, J. Marganec-Galkazka, A. Movsesyan, E. Nacher, E. Y. Nikolskii, T. Nilsson, C. Nociforo, A. Perea, M. Petri, S. Pietri, R. Plag, R. Reifarth, G. Ribeiro, C. Rigollet, D. M. Rossi, M. Röder, D. Savran, H. Scheit, H. Simon, O. Sorlin, I. Syndikus, J. T. Taylor, O. Tengblad, R. Thies, Y. Togano, M. Vandebrouck, P. Velho, V. Volkov, A. Wagner, F. Wamers, H. Weick, C. Wheldon, G. L. Wilson, J. S. Winfield, P. Woods, D. Yakorev, M. Zhukov, A. Zilges, and K. Zuber, “Quasifree  $(p, 2p)$  reactions on oxygen isotopes: Observation of isospin independence of the reduced single-particle strength,” *Phys. Rev. Lett.*, vol. 120, p. 052501, Jan 2018.
- [30] J.-J. Gaimard and K.-H. Schmidt, “A reexamination of the abrasion-ablation model for the description of the nuclear fragmentation reaction,” *Nuclear Physics A*, vol. 531, no. 3, pp. 709 – 745, 1991.
- [31] W.-M. Y. et al, “Review of particle physics,” *Journal of Physics G: Nuclear and Particle Physics*, vol. 33, no. 1, p. 1, 2006.

- 
- [32] R. Hollinger, K. Tinschert, J. Pfister, A. Adonin, R. Berezov, M. Brühl, B. Gutermuth, F. Heymach, R. Lang, J. Mäder, J. Maimone, K. Ochs, J. Roßbach, P. Schäffer, S. Schäffer, S. Stork, C. Vierheller, A. Wesp, and S. Zulauf, *Ion Source Operation at the GSI Accelerator Facility*, vol. 2013-1 of *GSI Report*. Darmstadt: GSI Helmholtzzentrum für Schwerionenforschung, 2013.
- [33] H. Geissel, P. Armbruster, K. Behr, A. Brünle, K. Burkard, M. Chen, H. Folger, B. Franczak, H. Keller, O. Klepper, B. Langenbeck, F. Nickel, E. Pfeng, M. Pfützner, E. Roeckl, K. Rykaczewski, I. Schall, D. Schardt, C. Scheidenberger, K.-H. Schmidt, A. Schröter, T. Schwab, K. Sümmerer, M. Weber, G. Münzenberg, T. Brohm, H.-G. Clerc, M. Fauerbach, J.-J. Gaimard, A. Grewe, E. Hanelt, B. Knödler, M. Steiner, B. Voss, J. Weckenmann, C. Ziegler, A. Magel, H. Wollnik, J. Dufour, Y. Fujita, D. Vieira, and B. Sherrill, “The GSI projectile fragment separator (FRS): a versatile magnetic system for relativistic heavy ions,” *Nuclear Instruments and Methods in Physics Research Section B: Beam Interactions with Materials and Atoms*, vol. 70, no. 1, pp. 286 – 297, 1992.
- [34] B. Voss, T. Brohm, H.-G. Clerc, A. Grewe, E. Hanelt, A. Heinz, M. de Jong, A. Junghans, W. Morawek, C. Röhl, S. Steinhäuser, C. Ziegler, K.-H. Schmidt, K.-H. Behr, H. Geissel, G. Münzenberg, F. Nickel, C. Scheidenberger, K. Sümmerer, A. Magel, and M. Pfützner, “The scintillation-detector equipment of the GSI projectile—fragment separator,” *Nuclear Instruments and Methods in Physics Research Section A: Accelerators, Spectrometers, Detectors and Associated Equipment*, vol. 364, no. 1, pp. 150 – 158, 1995.
- [35] V. Metag, R. Fischer, W. Kühn, R. Mühlhans, R. Novotny, D. Habs, U. Helmolt, H. Heyng, R. Kroth, D. Pelte, D. Schwalm, W. Hennerici, H. Hennrich, G. Himmele, E. Jaeschke, R. Repnow, W. Wahl, E. Adelberger, A. Lazzarini, R. Simon, R. Albrecht, and B. Kolb, “Physics with  $4\pi$ - $\gamma$ -detectors,” *Nuclear Physics A*, vol. 409, pp. 331 – 342, 1983.
- [36] K. Mahata, H. Johansson, S. Paschalis, H. Simon, and T. Aumann, “Position reconstruction in large-area scintillating fibre detectors,” *Nuclear Instruments and Methods in Physics Research Section A: Accelerators, Spectrometers, Detectors and Associated Equipment*, vol. 608, no. 2, pp. 331 – 335, 2009.
- [37] T. Blaich *et al.*, “A large area detector for high-energy neutrons,” *Nuclear Instruments and Methods in Physics Research A*, vol. 314, pp. 136–154, 1992.

- [38] Y. Yano, “The RIKEN RI beam factory project: A status report,” *Nuclear Instruments and Methods in Physics Research Section B: Beam Interactions with Materials and Atoms*, vol. 261, no. 1, pp. 1009 – 1013, 2007. The Application of Accelerators in Research and Industry.
- [39] T. Kubo, “In-flight RI beam separator BigRIPS at RIKEN and elsewhere in Japan,” *Nuclear Instruments and Methods in Physics Research Section B: Beam Interactions with Materials and Atoms*, vol. 204, pp. 97 – 113, 2003. 14th International Conference on Electromagnetic Isotope Separators and Techniques Related to their Applications.
- [40] T. Kobayashi, N. Chiga, T. Isobe, Y. Kondo, T. Kubo, K. Kusaka, T. Motobayashi, T. Nakamura, J. Ohnishi, H. Okuno, H. Otsu, T. Sako, H. Sato, Y. Shimizu, K. Sekiguchi, K. Takahashi, R. Tanaka, and K. Yoneda, “SAMURAI spectrometer for RI beam experiments,” *Nuclear Instruments and Methods in Physics Research Section B: Beam Interactions with Materials and Atoms*, vol. 317, pp. 294 – 304, 2013. XVIth International Conference on ElectroMagnetic Isotope Separators and Techniques Related to their Applications, December 2–7, 2012 at Matsue, Japan.
- [41] S. Takeuchi, T. Motobayashi, Y. Togano, M. Matsushita, N. Aoi, K. Demichi, H. Hasegawa, and H. Murakami, “DALI2: A NaI(Tl) detector array for measurements of  $\gamma$  rays from fast nuclei,” *Nuclear Instruments and Methods in Physics Research Section A: Accelerators, Spectrometers, Detectors and Associated Equipment*, vol. 763, pp. 596 – 603, 2014.
- [42] Y. Kondo, T. Nakamura, Y. Kawada, T. Sako, R. Tanaka, S. Deguchi, N. Kobayashi, G. Lee, K. Takahashi, and Y. Satou, *NEBULA (Neutron detection system for breakup of unstable nuclei with large acceptance*, vol. 44. RIKEN Nishina Center, 2011.
- [43] O. Sorlin and M.-G. Porquet, “Nuclear magic numbers: New features far from stability,” *Progress in Particle and Nuclear Physics*, vol. 61, no. 2, pp. 602 – 673, 2008.
- [44] H. Liu, J. Lee, P. Doornenbal, H. Scheit, S. Takeuchi, N. Aoi, K. Li, M. Matsushita, D. Steppenbeck, H. Wang, H. Baba, E. Ideguchi, N. Kobayashi, Y. Kondo, G. Lee, S. Michimasa, T. Motobayashi, A. Poves, H. Sakurai, M. Takechi, Y. Togano, J. Tostevin, and Y. Utsuno, “Intruder configurations in the ground state of  $^{30}\text{Ne}$ ,” *Physics Letters B*, vol. 767, pp. 58 – 62, 2017.
- [45] M. Wang, G. Audi, A. H. Wapstra, F. G. Kondev, M. MacCormick, X. Xu, and B. Pfeiffer, “The AME2012 atomic mass evaluation (II). tables, graphs and references,” *Chin.Phys.C*, vol. 36, p. 1603, 2012.



- 
- [46] N. Kobayashi, T. Nakamura, Y. Kondo, J. A. Tostevin, N. Aoi, H. Baba, R. Barthelemy, M. A. Famiano, N. Fukuda, N. Inabe, M. Ishihara, R. Kanungo, S. Kim, T. Kubo, G. S. Lee, H. S. Lee, M. Matsushita, T. Motobayashi, T. Ohnishi, N. A. Orr, H. Otsu, T. Sako, H. Sakurai, Y. Satou, T. Sumikama, H. Takeda, S. Takeuchi, R. Tanaka, Y. Togano, and K. Yoneda, “One-neutron removal from  $^{29}\text{Ne}$ : Defining the lower limits of the island of inversion,” *Phys. Rev. C*, vol. 93, p. 014613, Jan 2016.
- [47] M. Belleguic, F. Azaiez, Z. Dombrádi, D. Sohler, M. J. Lopez-Jimenez, T. Otsuka, M. G. Saint-Laurent, O. Sorlin, M. Stanoiu, Y. Utsuno, Y.-E. Penionzhkevich, N. L. Achouri, J. C. Angelique, C. Borcea, C. Bourgeois, J. M. Daugas, F. D. Oliveira-Santos, Z. Dlouhy, C. Donzaud, J. Duprat, Z. Elekes, S. Grévy, D. Guillemaud-Mueller, S. Leenhardt, M. Lewitowicz, S. M. Lukyanov, W. Mittig, M. G. Porquet, F. Pougheon, P. Roussel-Chomaz, H. Savajols, Y. Sobolev, C. Stodel, and J. Timár, “Search for neutron excitations across the  $N=20$  shell gap in  $^{25-29}\text{Ne}$ ,” *Phys. Rev. C*, vol. 72, p. 054316, Nov 2005.
- [48] S. Agostinelli, J. Allison, K. Amako, J. Apostolakis, H. Araujo, P. Arce, M. Asai, D. Axen, S. Banerjee, G. Barrand, F. Behner, L. Bellagamba, J. Boudreau, L. Broglia, A. Brunengo, H. Burkhardt, S. Chauvie, J. Chuma, R. Chytrcek, G. Cooperman, G. Cosmo, P. Degtyarenko, A. Dell’Acqua, G. Depaola, D. Dietrich, R. Enami, A. Feliciello, C. Ferguson, H. Fesefeldt, G. Folger, F. Foppiano, A. Forti, S. Garelli, S. Giani, R. Giannitrapani, D. Gibin, J. G. Cadenas, I. González, G. G. Abril, G. Greeniaus, W. Greiner, V. Grichine, A. Grossheim, S. Guatelli, P. Gumplinger, R. Hamatsu, K. Hashimoto, H. Hasui, A. Heikkinen, A. Howard, V. Ivanchenko, A. Johnson, F. Jones, J. Kallenbach, N. Kanaya, M. Kawabata, Y. Kawabata, M. Kawaguti, S. Kelner, P. Kent, A. Kimura, T. Kodama, R. Kokoulin, M. Kossov, H. Kurashige, E. Lamanna, T. Lampén, V. Lara, V. Lefebure, F. Lei, M. Liendl, W. Lockman, F. Longo, S. Magni, M. Maire, E. Medernach, K. Minamimoto, P. M. de Freitas, Y. Morita, K. Murakami, M. Nagematu, R. Nartallo, P. Nieminen, T. Nishimura, K. Ohtsubo, M. Okamura, S. O’Neale, Y. Oohata, K. Paech, J. Perl, A. Pfeiffer, M. Pia, F. Ranjard, A. Rybin, S. Sadilov, E. D. Salvo, G. Santin, T. Sasaki, N. Savvas, Y. Sawada, S. Scherer, S. Sei, V. Sirotenko, D. Smith, N. Starkov, H. Stoecker, J. Sulkimo, M. Takahata, S. Tanaka, E. Tcherniaev, E. S. Tehrani, M. Tropeano, P. Truscott, H. Uno, L. Urban, P. Urban, M. Verderi, A. Walkden, W. Wander, H. Weber, J. Wellisch, T. Wenaus, D. Williams, D. Wright, T. Yamada, H. Yoshida, and D. Zschesche, “Geant4—a simulation toolkit,” *Nuclear Instruments and Methods in Physics Research Section A: Accelerators, Spectrom-*

- ters, Detectors and Associated Equipment*, vol. 506, no. 3, pp. 250 – 303, 2003.
- [49] J. Mayer. Private communication, November 2017.
  - [50] The R<sup>3</sup>B Collaboration, “Technical Report for the Design, Construction and Commissioning of NeuLAND: The High-Resolution Neutron Time-of-Flight Spectrometer for R<sup>3</sup>B,” tech. rep., FAIR, November 2011. <http://www.fair-center.eu/fileadmin/fair/experiments/NUSTAR/Pdf/TDRs/NeuLAND-TDR-Web.pdf>.
  - [51] H. T. Johansson, “The GGLAND command-line simulation wrapper.” [http://fy.chalmers.se/~f96hajo/ggland/ggland\\_doc.pdf](http://fy.chalmers.se/~f96hajo/ggland/ggland_doc.pdf), 2013.
  - [52] A. M. Lane and R. G. Thomas, “R-matrix theory of nuclear reactions,” *Rev. Mod. Phys.*, vol. 30, pp. 257–353, Apr 1958.
  - [53] Y. Kondo, T. Nakamura, Y. Satou, T. Matsumoto, N. Aoi, N. Endo, N. Fukuda, T. Gomi, Y. Hashimoto, M. Ishihara, S. Kawai, M. Kitayama, T. Kobayashi, Y. Matsuda, N. Matsui, T. Motobayashi, T. Nakabayashi, T. Okumura, H. Ong, T. Onishi, K. Ogata, H. Otsu, H. Sakurai, S. Shimoura, M. Shinohara, T. Sugimoto, S. Takeuchi, M. Tamaki, Y. Togano, and Y. Yanagisawa, “Low-lying intruder state of the unbound nucleus <sup>13</sup>Be,” *Physics Letters B*, vol. 690, no. 3, pp. 245 – 249, 2010.
  - [54] P. Fallon, E. Rodriguez-Vieitez, D. Bazin, C. M. Campbell, J. M. Cook, R. M. Clark, D.-C. Dinca, A. Gade, T. Glasmacher, I.-Y. Lee, A. O. Macchiavelli, W. F. Mueller, S. G. Prussin, M. Wiedeking, and K. Yoneda, “Transition to the island of inversion: Study of excited states in 28-30Ne,” *Journal of Physics: Conference Series*, vol. 49, no. 1, p. 165, 2006.
  - [55] K. Sümmerer, “Improved empirical parametrization of fragmentation cross sections,” *Phys. Rev. C*, vol. 86, p. 014601, Jul 2012.
  - [56] K. Sümmerer, “Erratum: Improved empirical parametrization of fragmentation cross sections [phys. rev. c 86, 014601 (2012)],” *Phys. Rev. C*, vol. 87, p. 039903, Mar 2013.
  - [57] R. Thies, *Bits and pieces for the nuclear puzzle*. PhD thesis, Chalmers University of Technology, 2016.
  - [58] W. R. Webber, J. C. Kish, and D. A. Schrier, “Individual isotopic fragmentation cross sections of relativistic nuclei in hydrogen, helium, and carbon targets,” *Phys. Rev. C*, vol. 41, pp. 547–565, Feb 1990.



- 
- [59] J. M. Kidd, P. J. Lindstrom, H. J. Crawford, and G. Woods, “Fragmentation of carbon ions at 250 MeV/nucleon,” *Phys. Rev. C*, vol. 37, pp. 2613–2623, Jun 1988.
- [60] T. Ogawa, T. Sato, S. Hashimoto, D. Satoh, S. Tsuda, and K. Nita, “Energy-dependent fragmentation cross sections of relativistic  $^{12}\text{C}$ ,” *Phys. Rev. C*, vol. 92, p. 024614, Aug 2015.
- [61] H. T. Fortune, “ $(sd)^4$  states in  $^{12,14}\text{Be}$ ,” *Phys. Rev. C*, vol. 94, p. 064308, Dec 2016.
- [62] A. N. Ostrowski, H. G. Bohlen, A. S. Demyanova, B. Gebauer, R. Kalpakchieva, C. Langner, H. Lenske, M. von Lucke-Petsch, W. von Oertzen, A. A. Ogloblin, Y. E. Penionzhkevich, M. Wilpert, and T. Wilpert, “Mass spectroscopy of  $^{13}\text{Be}$ ,” *Zeitschrift für Physik A Hadrons and Nuclei*, vol. 343, pp. 489–490, Dec 1992.
- [63] A. Korshennikov, E. Nikolskii, T. Kobayashi, D. Aleksandrov, M. Fujimaki, H. Kumagai, A. Ogloblin, A. Ozawa, I. Tanihata, Y. Watanabe, and K. Yoshida, “Spectroscopy of  $^{12}\text{Be}$  and  $^{13}\text{Be}$  using a  $^{12}\text{Be}$  radioactive beam,” *Physics Letters B*, vol. 343, no. 1, pp. 53 – 58, 1995.
- [64] A. Belozorov, R. Kalpakchieva, Y. Penionzhkevich, Z. Dlouhy, S. Piskor, J. Vincour, H. Bohlen, M. von Lucke-Petsch, A. Ostrowski, D. Alexandrov, E. Nikolskii, B. Novatskii, and D. Stepanov, “Spectroscopy of  $^{13}\text{Be}$ ,” *Nuclear Physics A*, vol. 636, no. 4, pp. 419 – 426, 1998.
- [65] G. Randisi, A. Leprince, H. Al Falou, N. A. Orr, F. M. Marqués, N. L. Achouri, J.-C. Angélique, N. Ashwood, B. Bastin, T. Bloxham, B. A. Brown, W. N. Catford, N. Curtis, F. Delaunay, M. Freer, E. de Góes Brennand, P. Haigh, F. Hanappe, C. Harlin, B. Laurent, J.-L. Lecouey, A. Ninane, N. Patterson, D. Price, L. Stuttgé, and J. S. Thomas, “Structure of  $^{13}\text{Be}$  probed via secondary-beam reactions,” *Phys. Rev. C*, vol. 89, p. 034320, Mar 2014.
- [66] B. R. Marks, P. A. DeYoung, J. K. Smith, T. Baumann, J. Brown, N. Frank, J. Hinnefeld, M. Hoffman, M. D. Jones, Z. Kohley, A. N. Kuchera, B. Luther, A. Spyrou, S. Stephenson, C. Sullivan, M. Thoennessen, N. Viscariello, and S. J. Williams, “Population of  $^{13}\text{Be}$  in a nucleon exchange reaction,” *Phys. Rev. C*, vol. 92, p. 054320, Nov 2015.
- [67] A. T. Reed, O. Tarasov, R. D. Page, D. Guillemaud-Mueller, Y. E. Penionzhkevich, R. G. Allatt, J. C. Angélique, R. Anne, C. Borcea, V. Burjan, W. N. Catford, Z. Dlouhý, C. Donzaud, S. Grévy, M. Lewitowicz, S. M. Lukyanov, F. M. Marqués, G. Martinez, A. C. Mueller, P. J. Nolan, J. Novák, N. A. Orr, F. Pougheon, P. H. Regan,

- M. G. Saint-Laurent, T. Siiskonen, E. Sokol, O. Sorlin, J. Suhonen, W. Trinder, and S. M. Vincent, “Radioactivity of neutron-rich oxygen, fluorine, and neon isotopes,” *Phys. Rev. C*, vol. 60, p. 024311, Jul 1999.
- [68] A. Lepailleur, O. Sorlin, L. Caceres, B. Bastin, C. Borcea, R. Borcea, B. A. Brown, L. Gaudefroy, S. Grévy, G. F. Grinyer, G. Hagen, M. Hjorth-Jensen, G. R. Jansen, O. Llidoo, F. Negoita, F. de Oliveira, M.-G. Porquet, F. Rotaru, M.-G. Saint-Laurent, D. Sohler, M. Stanoiu, and J. C. Thomas, “Spectroscopy of  $^{26}\text{F}$  to probe proton-neutron forces close to the drip line,” *Phys. Rev. Lett.*, vol. 110, p. 082502, Feb 2013.
- [69] M. Stanoiu, D. Sohler, O. Sorlin, Z. Dombrádi, F. Azaiez, B. A. Brown, C. Borcea, C. Bourgeois, Z. Elekes, Z. Fülöp, S. Grévy, D. Guillemaud-Mueller, F. Ibrahim, A. Kerek, A. Krasznahorkay, M. Lewitowicz, S. M. Lukyanov, J. Mrázek, F. Negoita, Y.-E. Penionzhkevich, Z. Podolyák, M. G. Porquet, P. Roussel-Chomaz, M. G. Saint-Laurent, H. Savajols, G. Sletten, J. Timár, and C. Timis, “Spectroscopy of  $^{26}\text{F}$ ,” *Phys. Rev. C*, vol. 85, p. 017303, Jan 2012.
- [70] B. Jurado, H. Savajols, W. Mittig, N. Orr, P. Roussel-Chomaz, D. Baimborodin, W. Catford, M. Chartier, C. Demonchy, Z. Dlouhý, A. Gillibert, L. Giot, A. Khouaja, A. Lépine-Szily, S. Lukyanov, J. Mrázek, Y. Penionzhkevich, S. Pita, M. Rousseau, and A. Villari, “Mass measurements of neutron-rich nuclei near the  $N=20$  and  $28$  shell closures,” *Physics Letters B*, vol. 649, no. 1, pp. 43 – 48, 2007.
- [71] N. Frank, D. Albertson, J. Bailey, T. Baumann, D. Bazin, B. A. Brown, J. Brown, P. A. DeYoung, J. E. Finck, A. Gade, J. Hinnefeld, R. Howes, M. Kasperczyk, B. Luther, W. A. Peters, A. Schiller, A. Smith, M. Thoennessen, and J. A. Tostevin, “Neutron-unbound states in  $^{25,26}\text{F}$ ,” *Phys. Rev. C*, vol. 84, p. 037302, Sep 2011.
- [72] T. Rauscher, J. H. Applegate, J. J. Cowan, F.-K. Thielemann, and M. Wiescher, “Production of heavy elements in inhomogeneous cosmologies,” *APJ*, vol. 429, pp. 499–530, July 1994.
- [73] B. Meyer, “Webnucleo.org,” in *PoS (NIC XII)*, p. 096, 2012.